On the Joint Effect of Rain and Beam Misalignment in Terahertz Wireless Systems

ALEXANDROS-APOSTOLOS A. BOULOGEORGOS[1], (Senior Member, IEEE),
JOSÉ MANUEL RIERA[2], (Senior Member, IEEE), AND **ANGELIKI ALEXIOU**[1], (Member, IEEE)

[1]Department of Digital Systems, University of Piraeus, 18534 Piraeus, Greece
[2]Information Processing and Telecommunication Center, ETSI de Telecomunicación, Universidad Politécnica de Madrid, 28040 Madrid, Spain

Corresponding author: Alexandros-Apostolos A. Boulogeorgos (al.boulogeorgos@ieee.org)

ABSTRACT This contribution focuses on extracting the theoretical framework for the assessment and evaluation of the joint effect of rain, beam misalignment and hardware imperfections at long-range outdoor terahertz (THz) wireless systems. In this direction, we first report an appropriate system model for outdoor THz wireless systems that take into account the impact of different design parameters, including antenna gain and transceivers hardware imperfections, atmospheric conditions, such as rain, and parameters, like temperature, humidity and pressure, as well as stochastic beam misalignment that can be caused by thermal expansion, dynamic wind loads and/or weak earthquakes. For this model, we extract novel closed-form expressions for the probability density and cumulative distribution functions of the THz wireless channel that captures the impact of geometric loss, beam misalignment and rain attenuation. We capitalized the aforementioned expressions by presenting closed-form formulas for the outage probability and achievable throughput of the system. Finally, we document an analytical policy that returns the optimal transmission spectral efficiency that maximizes the achievable throughput.

INDEX TERMS Hardware imperfections, misalignment fading, outage probability, performance analysis, radio frequency chain imperfections, rain attenuation, statistical characterization, throughput, terahertz wireless systems, wireless fiber extender.

NOMENCLATURE

AWGN	Additive white Gaussian noise.
CCDF	Complementary cumulative distribution function.
CDF	Cumulative distribution function.
EVM	Error vector magnitude.
FSO	Free space optics.
HITRAN	High resolution transmission molecular absorption.
IR	Infrared.
ITU-R	International Telecommunication Union - Radiocommunication Sector.
OP	Outage probability.
PDF	Probability density function.
RF	Radio frequency.
RV	Random variable.
RX	Receiver.
SDNR	Signal-to-distortion-plus-noise-ratio.
SER	Symbol error rate.
THz	Terahertz.
SNR	Signal-to-noise-ratio.
THz	Terahertz.
TX	Transmitter.

I. INTRODUCTION

The terahertz (THz) band has been identified as a catalyst of the next generation communication era, since it offers comparable to the fiber experience and, as a consequence, enables a number of data rate hungry application scenarios, including wireless backhauling of remote areas and cost-efficient midhauling connectivity [1]–[7]. However, THz signals experience inherent high path-loss, due to their high transmission frequency as well as due to molecular absorption [8]–[13].

To counterbalance the severe path loss, high-directional antennas are employed at both the transmitter (TX) and the receiver (RX) [14], [15]. Unfortunately, directionality further complicates the establishment of the link, since perfect alignment between the transmission and reception beam is required [16], [17]. In practical implementations, this requirement can be met very rarely. The main reasons are physical phenomena, such as thermal expansion, dynamic wind loads, and weak earthquakes, that can cause a jitter at TX and RX antennas placed in high buildings [18], [19].

Recognizing this drawback, a great amount of research effort was put on analyzing, quantifying, and countermeasuring the impact of beam misalignment in THz wireless systems [4], [5], [20]–[26]. In more detail, in [20], the authors performed ray-tracing simulations in an realistic indoor environment in order to characterize the impact of beam misalignment, while, in [21], the antenna gain degradation due to stochastic misalignment in an indoor THz wireless system was quantified, assuming that the azimuth and elevation misalignment follow independent and identical Gaussian distributions. In [22], the authors experimentally evaluated the impact of deterministic beam misalignment in high-directional indoor THz wireless systems. In [23] and in [24], the impact of beam misalignment in indoor THz wireless systems operating at 100, 300, 400, and 500 GHz in terms of channel coefficient degradation were calculated by means of experimental measurements.

From the theoretical point of view, in [4], the impact of stochastic beam misalignment on the outage, error, and ergodic capacity performance of outdoor wireless THz systems that experience small and/or large scale fading was presented. Similarly, a closed-form expression for the error probability of mixed THz-radio frequency (RF) wireless systems, in which the THz link suffer from beam misalignment, was extracted in [5]. In [25], the authors documented a closed-form expression for the outage probability (OP) of wireless THz systems that experience fading, beam misalignment and phase noise. Finally, in [26], the authors presented novel closed-form expressions for the OP, error probabbility and ergodic capacity of THz wireless systems in the presence of stochastic beam misalignment and fog.

Another challenge, which outdoor THz wireless systems are facing, is received signal fluctuation under different weather conditions, i.e., weather-induced fading or, as it is called by both the THz the optical technology community scintillation [27], [28]. This phenomenon is generated as a consequence of the variation in the refraction index due to inhomogeneities in atmospheric temperature and pressure as well as water molecular density across the propagation path [29]. Weather-induced fading can dramatically affect the performance of THz wireless systems [30]. Motivated by this, several researchers have recently published a number of contributions concerning characterization, modeling, and analysis of the impact of different weather conditions on the performance of THz wireless systems [26], [31]–[40].

Specifically, in [31], the authors employed a weather emulating chamber in order to perform in-lab characterization of the impact of fog in both THz wireless systems and free space optics. Similarly, in [32], the propagation efficiency of broadband THz pulses through a dense fog by means of received signal strength was experimentally presented. In [26], closed-form expressions for the probability density function (PDF) and cumulative distribution function (CDF), in terms of I-function, which characterize the joint impact of fog and beam misalignment, were presented. Building upon these expressions, the OP, average symbol error rate (SER), and ergodic channel capacity were derived.

In [33], the authors presented an experimental comparison of the impact of laboratory-controlled rain on the received signal strength and error rate performance of THz and infrared (IR) wireless systems. Their analysis concluded in the very interesting result that THz are slightly more robust to the impact of rain compared to the corresponding IR free space optics (FSO) systems. In [34], a rain attenuation characterization for THz wireless systems was conducted. Likewise, in [35], an analytical assessment on physical layer security of a point-to-point THz wireless link in rain and snow with a potential eavesdropper locating outside of the legitimate link path was performed. In the aforementioned paper, the authors employed the Gunn-Marshall and Sekhon-Srivastava to model the snowdrop size, and the Marshall-Palmer as well as Weibull distributions to model the raindrop size.

In [36], an experimental comparison of the impact of turbulence in THz and IR wireless systems was documented. In [37], an analytical model that assess the overall impact of turbulence on THz systems was presented. Building upon this model, in [38], the authors extracted closed-form expression for the average error rate and channel capacity of THz wireless systems in the presence of turbulence, while, in [39], the authors statistically characterized the end-to-end channel of multi-RIS assisted THz wireless systems that experience turbulence. Finally, in [40], the joint impact of snow, turbulence, and beam misalignment on the bit error rate and channel capacity of THz wireless systems were quantified.

We also recall that another factor that needs to be taken into account in the modeling and assessment of THz wireless systems performance is the impact of transceivers hardware imperfections [41]–[43]. In general, the effect of transceivers hardware imperfections was evaluated in several contributions, including [44]–[53]. However, their detrimental effect on THz wireless systems were only recently examined [54]–[56]. In particular, in [54], the authors revealed the detrimental impact of transceivers hardware imperfections in the error performance of THz wireless fiber extenders. Moreover, in [55], the performance degradation due to transceiver hardware imperfections that operate at the 300 GHz band, were documented. Finally, in [56], the authors evaluated the impact of transceivers hardware imperfections in THz wireless systems that employ spatial modulation.

Despite of the paramount importance that the weather conditions, beam misalignment and transceivers hardware imperfections play on the performance of THz wireless systems, to the best of the authors knowledge only the joint impact of turbulence, beam misalignment and hardware imperfections in terms of OP has been so far investigated [39]. Towards filling this gap, in this paper, we investigate the joint impact of rain, beam misalignment and transceiver hardware imperfections in THz wireless systems. In more detail, the technical contribution of the paper can be summarized as follows:

- We present a suitable system model for outdoor THz wireless systems, which accounts the different design parameters and their interactions as well as the presence and absence of rain. The aforementioned parameters include the transmission distance, the transceivers antenna gains, the level of beam misalignment, the transmission power, the atmospheric temperature, pressure and relative humidity, the expected value and variance of rain attenuation as well as the probability of rain.
- In order to characterize the stochastic behavior of the THz wireless channel, we extract novel closed-form expressions for the PDF and CDF that captures the joint impact of geometric-loss, rain attenuation and beam-misalignment.
- Building upon the channel model, we present closed-form expressions for the OP and the system throughput. The derived expressions accommodate the impact of stochastic beam misalignment, rain as well as transceiver hardware imperfections. As a benchmark, simplified expressions for the case in which the THz wireless system suffers only from beam misalignment and transceiver hardware imperfections are also presented. Another theoretical benchmark that is reported is the special case in which, although it rains, the THz wireless system does not experience beam-misalignment. Note that this is an ideal non-realistic scenario, which allow us to quantify the severity of beam-misalignment.
- Finally, we present an analytical policy for selecting the optimum transmission spectral efficiency that maximizes the achievable throughput, for given transmission power, levels of transceiver hardware imperfection and rain attenuation.

The rest of this paper is organized as follows. Section II is devoted to the presentation of the system and channel models. The statistical characterization of the THz wireless channel is reported in Section III. Section IV focuses on documenting the performance metrics, namely signal-to-distortion-plus-noise-ratio (SDNR), OP, and throughput, as well as the throughput maximization policy. Numerical results and discussions are given in Section V. Finally, concluded remarks and observations are highlighted in Section VI. The organization of the paper in a glance is illustrated in Fig. 1.

Notations: The absolute value and the square root of t are respectively denoted by $|t|$ and $\sqrt{t}$. Moreover, t^n stands
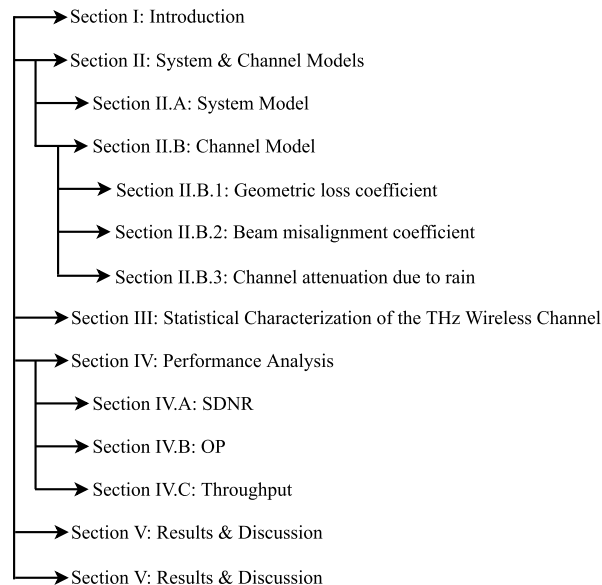
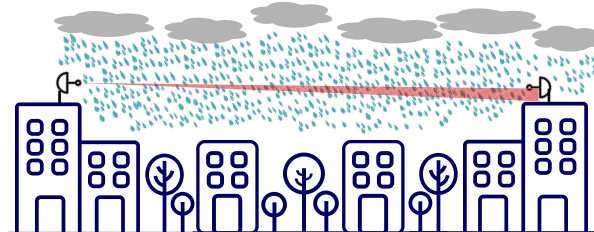**FIGURE 1.** Paper's structure at a glance.

FIGURE 2. System model.

for the x in the power of n. The natural logarithm and the base-n logarithm of t are respectively represented by $\ln(t)$ and $\log_n(t)$. The exponential and the tangent of t are respectively given by $\exp(t)$ and $\tan(t)$. The error function is denoted by $\mathrm{erf}(\cdot)$, while $\mathrm{erfc}(\cdot)$ stands for the complementary error function. Likewise, $t \sim \mathcal{CN}\left(\mu_t, \sigma_t^2\right)$ indicates that t is a random variable (RV) that follows complex Gaussian distribution with mean μ_t and variance σ_t^2. Finally, $\Pr(\mathcal{A})$ stands for the probability for the event $\mathcal{A}$ to be valid.

II. SYSTEM & CHANNEL MODELS

This section focuses on presenting the system and channel models. In particular, Section II-A reports the THz wireless fiber extender system model and lists all the transmission and reception parameters. Section II-B documents the THz wireless channel model and presents the interconnection between the channel coefficient and the communication parameters as well as the atmospheric and weather conditions.

A. SYSTEM MODEL

As depicted in Fig. 2, we consider a directional point-to-point THz wireless system, in which both the TX and RX are equipped with high directional antennas. The baseband equivalent received signal can be expressed as

$$r = h(s + \eta_t) + \eta_r + n, \tag{1}$$

TABLE 1. Parameters definition.

Parameters	
T	atmospheric temperature
P	atmospheric pressure
ϕ	relative humidity
c	Speed-of-light
f	Transmission frequency
d	Transmission distance
G_t	Transmission antenna gain
$\Theta_{3\text{dB}}$	Half-power beam-width of the TX antenna
G_r	Reception antenna gain
P_s	Average transmission signal power
α_r	radius of the effective area of the RX antenna
A_o	The portion of the collected power at the RX in the absence of beam misalignment
w_d	Beam waist at distance d
w_e	Equivalent beam-width
σ_s	spatial jitter standard deviation
μ_r	mean value of channel attenuation due to rain
σ_r^2	variance of channel attenuation due to rain
P_o	Probability of rain
A	rain attenuation lower-threshold
ρ	rain specific attenuation
R	rainfall rate
k_r	rain-related frequency- and polarization-dependent parameter
a_r	rain-related frequency- and polarization-dependent parameter
s	Transmission signal
h	THz wireless channel coefficient
h_l	Geometric loss coefficient
h_m	beam misalignment fading coefficient
h_r	rain attenuation coefficient
h_f	free space loss coefficient
h_g	molecular absorption loss coefficient
n	Additive white Gaussian noise
N_o	Variance of n
η_t	TX distortion noise
κ_t	TX EVM
η_r	RX distortion noise
κ_r	RX EVM
$\tilde{\gamma}_s$	Transmission SNR
γ_{th}	SNR threshold

where s stands for the transmission signal, while n represents the additional additive white Gaussian noise (AWGN), which can be modeled as a zero-mean Gaussian RV of variance N_o. Moreover, h denotes the channel coefficient and can be expressed as

$$h = h_l \, h_m \left((1 - \delta) + \delta \, h_r \right), \tag{2}$$

where h_l and h_m respectively stand for the geometric loss and the beam misalignment fading coefficients, while h_r is the rain channel attenuation coefficients. Moreover, δ is a binary RV that is defined as

$$\delta = \begin{cases} 1, & \text{if it rains} \\ 0, & \text{otherwise.} \end{cases} \tag{3}$$

for which

$$\Pr(\delta = 1) = P_o, \text{ and } \Pr(\delta = 0) = 1 - P_o, \tag{4}$$

with P_o being the probability of rain. Notice that P_o depends on the local climate at a specific observation period [57] and it can be generally estimated by following the procedure described in the Recommendation ITU-R P.837 [58].

Finally, the parameters η_t and η_r are the TX and RX distortion noises, due to the RF chain hardware imperfections.

Note that, according to [42], [59], [60],

$$\eta_t \sim \text{CN}\left(0, \kappa_t^2 P_s\right), \text{ and } \eta_t \sim \text{CN}\left(0, \kappa_r^2 h^2 P_s\right), \tag{5}$$

with κ_t and κ_r being the error vector magnitudes (EVMs) of the TX and RX, respectively [49], [51], [61]–[63]. Of note, EVM is a common quality metric of the RF transceiver's quality and is defined as the ratio of the average distortion magnitude to the average signal magnitude. As reported in [4], in THz wireless systems κ_t and κ_r are in the range of $[0, 0.4]$. Notice that $\kappa_t = \kappa_r = 0$ corresponds to the ideal RF front-end case. Finally, P_s denotes the average transmission power.

B. CHANNEL MODEL
The objective of this section is to present the channel model. Towards this direction, the geometric loss model is discussed in Section II-B1, whereas, the beam misalignment model is reported in Section II-B2. Finally, Section II-B3 provides the model for the rain attenuation coefficient.

1) GEOMETRIC LOSS COEFFICIENT
The geometric loss coefficient can be further analyzed as

$$h_l = h_f \, h_g, \tag{6}$$

where h_f models the free space losses and can be evaluated, based on the Friis equation, as

$$h_f = \frac{c\sqrt{G_t \, G_r}}{4\pi f \, d}, \tag{7}$$

where G_t and G_r are the transmission and reception antenna gains, respectively, while c and f are respectively the speed of light and the transmission frequency. Finally, d stands for the transmission distance.

In addition, h_g is the molecular absorption channel coefficient, which can be calculated as

$$h_g = \exp\left(-\frac{1}{2}\kappa_a\left(T, \phi, P\right) d\right), \tag{8}$$

with $\kappa_a\left(T, P, \phi\right)$ being the molecular absorption coefficient. The molecular absorption coefficient depends on the atmospheric temperature, T, and pressure, P, as well as the relative humidity, ϕ, and can be evaluated by leveraging the radiative transfer theory and the measured data provided in the high resolution transmission molecular absorption (HITRAN) database [64], as described in [8], [65], [66]. Alternative approaches to extract the molecular absorption coefficient by means of analytical formulas are provided in [67]–[69].

2) BEAM MISALIGNMENT CHANNEL COEFFICIENT
The beam misalignment channel coefficient is a RV. The PDF and CDF of h_m^2 can be respectively expressed as

$$f_{h_m^2}(x) = \begin{cases} \dfrac{\xi}{A_o^\xi} x^{\xi-1}, & 0 \le x \le A_o \\ 0, & \text{otherwise} \end{cases} \tag{9}$$

and

$$F_{h_m^2}(x) = \begin{cases} 0, & x < 0 \\ \dfrac{x^\xi}{A_o^\xi}, & 0 \le x \le A_o \\ 1, & x > A_o, \end{cases} \tag{10}$$

where A_o is the portion of the collected power by the RX in the absence of beam misalignment fading, and is given by

$$A_o = (\mathrm{erf}(v))^2, \tag{11}$$

with

$$v = \sqrt{\frac{\pi}{2}} \frac{\alpha_r}{w_d}. \tag{12}$$

In (12), α_r is the radius of the effective area of the reception antenna, which, according to [70, eqs. (2-117) and (2-119)] can be expressed as

$$\alpha_r = \frac{c\sqrt{G_r}}{2\pi f}. \tag{13}$$

Likewise, w_d stands for the beam waist at distance d and can be evaluated as

$$w_d = d \, \tan\left(\frac{\Theta_{3\mathrm{dB}}}{2}\right), \tag{14}$$

with $\Theta_{3\mathrm{dB}}$ being the half-power beamwidth of the transmission antenna. Note that based on the antenna transmission type $\Theta_{3\mathrm{dB}}$ is connected to the antenna gain with a one-to-one relationship. In particular, for the case in which the TX employs a Cassegrain antenna, the following formula is satisfied [70]:

$$\Theta_{3\mathrm{dB}} = \sqrt{\frac{4\pi}{G_t}}. \tag{15}$$

Moreover, in (9) and (10)

$$\xi = \frac{1}{4} \frac{w_e^2}{\sigma_s^2}, \tag{16}$$

where σ_s stands for the spatial jitter standard deviation, and w_e is the equivalent beamwidth that can be obtained as

$$w_e^2 = \sqrt{\pi} w_d^2 \frac{\mathrm{erf}(v)\exp\left(v^2\right)}{2v}. \tag{17}$$

3) CHANNEL ATTENUATION DUE TO RAIN

According to [71], the channel attenuation due to rain, h_r^2, can be accurately modeled as a log-normal distribution with mean and variance μ_r and σ_r^2, respectively. As a consequence, the PDF and CDF of h_r^2 can be respectively expressed as

$$f_{h_r^2}(x) = \frac{1}{\sqrt{2\pi}\sigma_r} x^{-1} \exp\left(-\frac{(\ln(x) - \mu_r)^2}{2\sigma_r^2}\right) \tag{18}$$

and

$$F_{h_r^2}(x) = \frac{1}{2} \mathrm{erfc}\left(\frac{\mu_r - \ln(x)}{\sqrt{2}\sigma_r}\right). \tag{19}$$

Notice that in this work, we use a log-normal distribution to model the attenuation conditioned to the presence of rain. Moreover, note that μ_r and σ_r depend on the local climate and the link characteristics, such as transmission distance, operation frequency, as well as polarization of the electromagnetic wave. Ideally, μ_r and σ_r should be obtained as a result of a fitting problem to rain attenuation measurements. However, since experimental rain attenuation datasets are not usually available for THz frequencies, as described in [72] and in [73], we employ the following procedure in order to evaluate μ_r and σ_r.

By employing the Dirac-lognormal model and leveraging (19), the probability that rain attenuation exceeds a lower-threshold, A, can be expressed as in [73]

$$P_A = \Pr\left(h_r^2 \ge A\right) = \frac{P_o}{2} \mathrm{erfc}\left(\frac{\ln(A) - \mu_r}{\sqrt{2}\sigma_r}\right). \tag{20}$$

In relatively-short distance (less than some decades of km) terrestrial THz wireless systems, it can be assumed that rainfall rate is homogeneous in the path. As a consequence, it can be estimated by evaluating the rain specific attenuation, ρ that is measured in dB/km, for a corresponding rainfall rate, R, measured in mm/h, and multiply by the transmission distance, d, measured in km, i.e.

$$A = \rho \, d, \tag{21}$$

which based on the ITU-R Recommendation P.838-3 [74], can be rewritten as

$$A = k_r \, R^{a_r} \, d. \tag{22}$$

In (22), κ_r and a_r are frequency- and polarization-dependent parameters provided in [74] for frequencies between 1 and 1000 GHz.

The procedure that we followed in this contribution in order to derive P_o, μ_r, and σ_r for the desired frequency and site, starts by obtaining the complementary CDF (CCDF) of rainfall rate P_o for the site using the model of ITU-R Rec. P.837-7 [75], which provides rainfall rate distributions for every location in the world for propagation modeling purposes. The probability of rain presence $P_{0,r}$ is also provided. Assuming the links are relatively short, i.e., less than 1 km, (22) is used to convert each R value associated to a probability into an A value associated to the same probability, and the probability of having rain attenuation present is made equal to the probability of rain presence, i.e. $P_o = P_{0,r}$. Then, the parameters μ_r and σ_r of the log-normal distribution are calculated by fitting the distribution P_A obtained from $\Pr(x \le R)$ to a distribution with the form of (20), using the procedure described in Annex 2 of ITU-R Rec. P.1057-6 [76].

III. STATISTICAL CHARACTERIZATION OF THE THz WIRELESS CHANNEL

The following Lemmas presents closed-form expressions for the PDF and CDF of h^2 in the absence and presence of rain.

Lemma 1: In the absence of rain, the PDF and CDF of h^2 can be respectively obtained as

$$f_{h^2|\delta=0}(x) = \begin{cases} \dfrac{\xi}{h_t^{2\xi} A_o^\xi} x^{\xi-1}, & for\ 0 \le x \le A_o h_t^2 \\ 0, & otherwise \end{cases} \quad (23)$$

and

$$F_{h^2|\delta=0}(x) = \begin{cases} 0, & x < 0 \\ \dfrac{x^\xi}{h_t^{2\xi} A_o^\xi}, & 0 \le x \le A_o h_t^2 \\ 1, & x > A_o h_t^2 \end{cases} \quad (24)$$

Proof: For brevity, the proof of Lemma 1 is provided in Appendix A. ∎

Lemma 2: In the presence of rain, the PDF and CDF of h^2 can be respectively obtained as

$$f_{h^2|\delta=1}(x)$$
$$= \frac{1}{2} \frac{\xi}{A_o^\xi} \exp\left(\frac{\sigma_r^2 \xi^2}{2} - \frac{\xi \mu_r}{\sigma_r}\right) \left(\frac{x}{h_t^2}\right)^{\xi-1}$$
$$\times \mathrm{erfc}\left(\frac{\sigma_r}{\sqrt{2}}\left(\xi - \frac{\mu_r}{\sigma_r^2}\right) + \frac{1}{\sqrt{2}\sigma_r} \ln\left(\frac{x}{A_o h_t^2}\right)\right). \quad (25)$$

and (26), as shown at the bottom of the page.

Proof: For brevity, the proof is provided in Appendix B. ∎

Proposition 1: The PDF and CDF of h^2 can be respectively obtained as

$$f_{h^2}(x) = (1 - P_o) f_{h^2|\delta=0}(x) + P_o f_{h^2|\delta=1}(x) \quad (27)$$

and

$$F_{h^2}(x) = (1 - P_o) F_{h^2|\delta=0}(x) + P_o F_{h^2|\delta=1}(x). \quad (28)$$

Proof: Since δ is a discrete RV and independent from h_r and h_m, by employing the Bayes theorem [77], we can respectively express the PDF and CDF of h^2 as

$$f_{h^2}(x) = \Pr(\delta = 0) f_{h^2|\delta=0}(x) + \Pr(\delta = 1) f_{h^2|\delta=1}(x) \quad (29)$$

and

$$F_{h^2}(x) = \Pr(\delta = 0) F_{h^2|\delta=0}(x)$$
$$+ \Pr(\delta = 1) F_{h^2|\delta=1}(x). \quad (30)$$

By applying (4) into (29) and (30), we respectively obtain (27) and (28), respectively. ∎

IV. PERFORMANCE ANALYSIS

Building upon the statistical characterization framework presented in III, in this section, we present novel closed-form expressions for the OP and the achievable throughput. Specifically, the rest of the section is organized as: in Section IV-A, the instantaneous SDNR is presented, while, in Section IV-B, the OP is derived. Finally, the achievable throughput is given in Section IV-C.

A. SDNR

From (1), the instantaneous SDNR at the receiver can be evaluated as

$$\gamma = \frac{h^2 P_s}{\left(\kappa_t^2 + \kappa_r^2\right) h^2 P_s + N_o}. \quad (31)$$

Note that in the ideal RF-case, where $\kappa_t = \kappa_r = 0$, (31) can be simplified to

$$\gamma_{\mathrm{id}} = \frac{h^2 P_s}{N_o}. \quad (32)$$

B. OP

The following proposition returns a closed-form expression for the OP.

Proposition 2: The OP can be obtained as in (33), as shown at the bottom of the next page. In (33),

$$\tilde{\gamma} = \frac{P_s}{N_o} \quad (34)$$

and γ_{th} stands for the SNR threshold.

Proof: For brevity, the proof of Proposition 3 is provided in Appendix C. ∎

1) SPECIAL CASE 1

In the absence of rain, but in the presence of beam misalignment, the OP can be evaluated from (33), by setting $P_o = 1$, as

$$P_{\mathrm{out}}^{\mathrm{nr}}(\gamma_{\mathrm{th}}) = \begin{cases} F_{h^2|\delta=0}\left(\dfrac{1}{1 - \gamma_{\mathrm{th}}(\kappa_t^2 + \kappa_r^2)} \dfrac{\gamma_{\mathrm{th}}}{\tilde{\gamma}}\right), & \text{for } \gamma_{\mathrm{th}} < \dfrac{1}{\kappa_t^2 + \kappa_r^2}, \\ 1, & \text{otherwise} \end{cases} \quad (35)$$

2) SPECIAL CASE 2

In the presence of both rain and beam misalignment, the OP can be evaluated from (33), by setting $P_o = 0$, as

$$P_{\mathrm{out}}^{\mathrm{r}}(\gamma_{\mathrm{th}}) = \begin{cases} F_{h^2|\delta=1}\left(\dfrac{1}{1 - \gamma_{\mathrm{th}}(\kappa_t^2 + \kappa_r^2)} \dfrac{\gamma_{\mathrm{th}}}{\tilde{\gamma}}\right), & \text{for } \gamma_{\mathrm{th}} < \dfrac{1}{\kappa_t^2 + \kappa_r^2}, \\ 1, & \text{otherwise} \end{cases} \quad (36)$$

$$F_{h^2|\delta=1}(x) = \frac{1}{2 A_o^\xi} \exp\left(\xi \ln(A_o) - \frac{\sigma_r^2 \xi^2}{2}\right) \left(\exp\left(\frac{\sigma_r^2 \xi^2}{2}\right) \mathrm{erfc}\left(\frac{\sqrt{2}}{2\sigma_r}\left(\mu_r - \ln\left(\frac{x}{h_t^2 A_o}\right)\right)\right)\right.$$
$$\left. + \exp\left(\sigma_r^2 \xi^2 + \xi \ln\left(\frac{x}{A_o h_t^2}\right)\right) \mathrm{erfc}\left(\frac{\sqrt{2}\sigma_r}{2}\left(\xi - \frac{\mu_r}{\sigma_r^2}\right) + \frac{1}{\sqrt{2}\sigma_r} \ln\left(\frac{x}{h_t^2 A_o}\right)\right)\right) \quad (26)$$

3) SPECIAL CASE 3 (IDEAL RF FRONT)

In the special and ideal case in which both the TX and RX are equipped with ideal RF front-ends, i.e., $\kappa_t = \kappa_r = 0$, (33) can be simplified as

$$P_{\text{out}}^{\text{id}}(\gamma_{\text{th}}) = (1 - P_o) \, F_{h^2|\delta=0} \left(\frac{\gamma_{\text{th}}}{\tilde{\gamma}} \right)$$
$$+ P_o \, F_{h^2|\delta=1} \left(\frac{\gamma_{\text{th}}}{\tilde{\gamma}} \right) \quad (37)$$

By comparing (33) and (37) and taking into account that the spectral efficiency and the SNR threshold are connected through

$$r_{\text{th}} = \log_2(1 + \gamma_{\text{th}}), \quad (38)$$

it becomes evident that the hardware imperfections creates a spectral efficiency upper bound beyond which the OP becomes equal to 1.

C. THROUGHPUT

The throughput can be obtained as

$$D(\gamma_{\text{th}}) = (1 - P_{\text{out}}(\gamma_{\text{th}})) \log_2(1 + \gamma_{th}). \quad (39)$$

The following proposition returns the optimal SNR threshold, γ_{th}^o, that maximizes the achieved throughput.

Proposition 3: The optimal SNR threshold, γ_{th}^o, that maximizes the achievable throughput is the solution of (40), as shown at the bottom of the page.

Proof: For brevity, the proof of Proposition 3 is provided in Appendix D. ∎

Note that (40) is very difficult or even impossible to be analytically solved. However, γ_{th}^o can be obtained by applying low-complexity numerical approaches, such as the Newton's method [78]. Finally, note that by applying (38) to the solution of (40), the optimal spectral efficiency of the transmission scheme can be extracted.

1) SPECIAL CASE 1

In the absence of rain, but in the presence of beam misalignment, (40) can be simplified as in (41), as shown at the bottom of the page.

2) SPECIAL CASE 2

In the presence of both rain and beam misalignment, (40) can be simplified as in (42), as shown at the bottom of the page.

3) SPECIAL CASE 3 (IDEAL RF FRONT-END)

In the special and ideal case in which both the TX and RX are equipped with ideal RF front-ends, i.e., $\kappa_t = \kappa_r = 0$, (40) can be simplified as

$$\frac{P_{\text{out}}\left(\gamma_{\text{th}}^{o,\text{id}}\right)}{\ln(2)\left(1 + \gamma_{\text{th}}^{o,\text{id}}\right)} = \frac{\log_2\left(1 + \gamma_{\text{th}}^{o,\text{id}}\right)}{\tilde{\gamma}} f_{h^2}\left(\frac{\gamma_{\text{th}}^{o,\text{id}}}{\tilde{\gamma}}\right), \quad (43)$$

where $\gamma_{\text{th}}^{o,\text{id}}$ stands for the optimal SNR threshold for the ideal RF front-end case.

$$P_{\text{out}}(\gamma_{\text{th}}) = \begin{cases} (1 - P_o) \, F_{h^2|\delta=0} \left(\frac{1}{1 - \gamma_{\text{th}}\left(\kappa_t^2 + \kappa_r^2\right)} \frac{\gamma_{\text{th}}}{\tilde{\gamma}} \right) + P_o \, F_{h^2|\delta=1} \left(\frac{1}{1 - \gamma_{\text{th}}\left(\kappa_t^2 + \kappa_r^2\right)} \frac{\gamma_{\text{th}}}{\tilde{\gamma}} \right), & \text{for } \gamma_{\text{th}} < \frac{1}{\kappa_t^2 + \kappa_r^2}, \\ 1, & \text{otherwise} \end{cases}$$

$$(33)$$

$$\frac{P_{\text{out}}\left(\gamma_{\text{th}}^o\right)}{\ln(2)\left(1 + \gamma_{\text{th}}^o\right)} = \log_2\left(1 + \gamma_{\text{th}}^o\right) \left(\frac{1}{\tilde{\gamma}\left(1 - \left(\kappa_t^2 + \kappa_r^2\right)\gamma_{\text{th}}^o\right)} + \gamma_{\text{th}}^o \frac{\kappa_t^2 + \kappa_r^2}{\tilde{\gamma}\left(1 - \left(\kappa_t^2 + \kappa_r^2\right)\gamma_{\text{th}}^o\right)^2} \right) f_{h^2}\left(\frac{\gamma_{\text{th}}^o}{\tilde{\gamma}\left(1 - \left(\kappa_t^2 + \kappa_r^2\right)\gamma_{\text{th}}^o\right)} \right)$$

$$(40)$$

$$\frac{P_{\text{out}}^{nr}\left(\gamma_{\text{th}}^o\right)}{\ln(2)\left(1 + \gamma_{\text{th}}^o\right)} = \log_2\left(1 + \gamma_{\text{th}}^o\right) \left(\frac{1}{\tilde{\gamma}\left(1 - \left(\kappa_t^2 + \kappa_r^2\right)\gamma_{\text{th}}^o\right)} + \gamma_{\text{th}}^o \frac{\kappa_t^2 + \kappa_r^2}{\tilde{\gamma}\left(1 - \left(\kappa_t^2 + \kappa_r^2\right)\gamma_{\text{th}}^o\right)^2} \right) f_{h^2|\delta=0}\left(\frac{\gamma_{\text{th}}^o}{\tilde{\gamma}\left(1 - \left(\kappa_t^2 + \kappa_r^2\right)\gamma_{\text{th}}^o\right)} \right)$$

$$(41)$$

$$\frac{P_{\text{out}}^{r}\left(\gamma_{\text{th}}^o\right)}{\ln(2)\left(1 + \gamma_{\text{th}}^o\right)} = \log_2\left(1 + \gamma_{\text{th}}^o\right) \left(\frac{1}{\tilde{\gamma}\left(1 - \left(\kappa_t^2 + \kappa_r^2\right)\gamma_{\text{th}}^o\right)} + \gamma_{\text{th}}^o \frac{\kappa_t^2 + \kappa_r^2}{\tilde{\gamma}\left(1 - \left(\kappa_t^2 + \kappa_r^2\right)\gamma_{\text{th}}^o\right)^2} \right) f_{h^2|\delta=1}\left(\frac{\gamma_{\text{th}}^o}{\tilde{\gamma}\left(1 - \left(\kappa_t^2 + \kappa_r^2\right)\gamma_{\text{th}}^o\right)} \right)$$
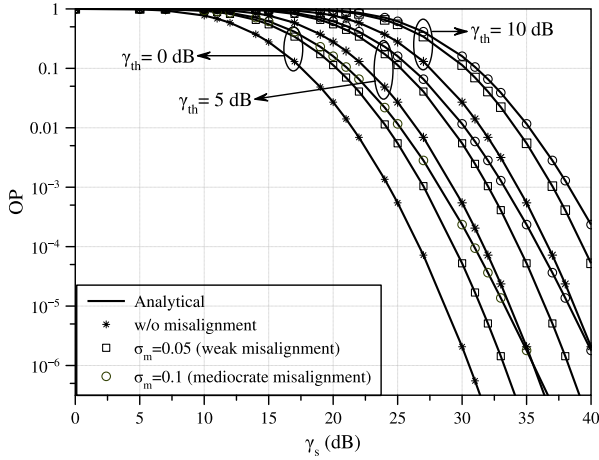
$$(42)$$

FIGURE 3. OP vs γ_s, for different levels of σ_m, and γ_{th}.

FIGURE 4. OP vs P_o, for different levels of σ_m, and $\gamma_s/\gamma_{\text{th}}$.

V. RESULTS & DISCUSSION

This section focuses on verifying the analytical framework that was documented in Section IV through Monte Carlo simulations.In this directions, unless otherwise stated, lines and markers are used for analytical results and simulations, respectively. The following scenario is considered. The transmission frequency and distance are set to 120 GHz and 100 m, respectively. The relative humidity, atmospheric pressure, and temperature are 50%, 101325 Pa, and 296 ^{o}K. Finally, both the TX and RX antenna gains are 55 dBi.

The rest of the section is organized as: In Section V-A, the joint impact of rain and misalignment is quantified assuming that both the TX and the RX are equipped with ideal RF front-ends, i.e. $\kappa_t = \kappa_r = 0$. Section V-B documents the joint impact of transceivers hardware imperfections, rain, and beam misalignment on the outage and throughput performance of THz wireless systems.

A. IDEAL RF FRONT-END

Figure 3 quantifies the impact of beam misalignment on the outage performance of a THz wireless system that operates under rain. In more detail, the OP is plotted as a function of the transmission SNR, γ_s, for different values of γ_{th} and σ_m, assuming that $\mu_r = -2.04$ and $\sigma_r = 0.86$. Note that the aforementioned values correspond on raining conditions in Athens, Greece, for transmission distance that equals 100 m. Moreover, we assume that $P_o = 1$. This indicates that we assess the THz wireless system performance for an observation period that is raining. As a benchmark, in this figure, we also presented the outage performance in the absence of misalignment. We observe that, for fixed σ_m and γ_{th}, as γ_s increases, the OP decreases. For example, for $\sigma_m = 0.05$ and $\gamma_{\text{th}} = 0$ dB, as γ_s increases from 25 to 30 dB, an approximately two orders of magnitude OP improvement is observed. Moreover, for given γ_s and σ_m, as γ_{th} increases, i.e. as the spectral efficiency of the transmission scheme increases, the OP also increases. For instance, for $\gamma_s = 25$ dB and $\sigma_m = 0.05$,the OP increases for one order of magnitude, as the γ_{th} changes from 0 to
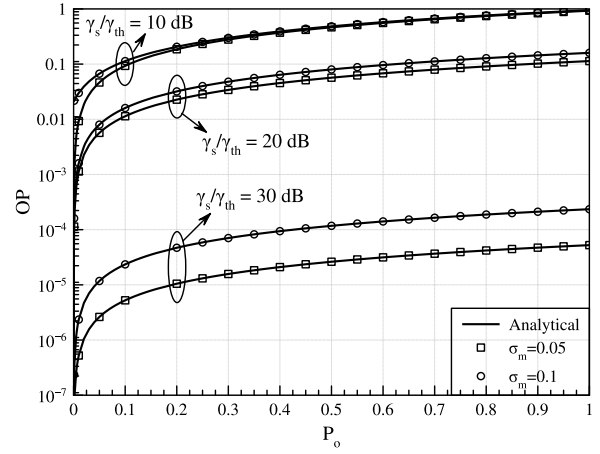
5 dB. From this figure, it also becomes apparent that, for fixed γ_s and γ_{th}, the outage performance degrades as the level of beam misalignment, i.e. σ_m, increases. For example, for $\gamma_s = 25$ dB and $\gamma_{\text{th}} = 0$ dB, the OP increases from 5.5×10^{-3} to 1.16×10^{-2}, as σ_m increases from 0.05 to 0.1. Finally, the importance of accounting the impact of misalignment when assessing the performance of THz wireless systems is highlighted. For instance, for $\gamma_s = 30$ dB, $\gamma_{\text{th}} = 0$ dB and $\sigma_m = 0.1$, an outage performance evaluation error that is greater than two orders of magnitude occurs, if the impact of beam-misalignment is not taken into consideration. This indicates that neglecting the impact of beam misalignment when evaluating the OP of THz wireless systems may lead to important assessment errors.

Figure 4 presents the OP as a function of P_o for different values of $\gamma_s/\gamma_{\text{th}}$ and σ_m, assuming that $\mu_r = -2.04$ and $\sigma_r = 0.86$. As described in Section II-B3, the parameters μ_r, σ_r and P_o are interdependent climate parameters that are affected by the observation period. However, in order to present the generality of the presented analysis and to derive some useful insights that connects the outage performance with the probability of rain, in this figure, we fix the parameters μ_r and σ_r, and quantify the OP for different values of P_o. Furthermore, notice that $P_o = 0$ refers to the case in which the THz wireless system suffers only from beam misalignment. As expected, for given P_o and $\gamma_s/\gamma_{\text{th}}$, the OP increases, as σ_m increases. For example, for $P_o = 0.5$ and $\gamma_s/\gamma_{\text{th}} = 30$ dB, the OP increases from 2.62×10^{-5} to 1.17×10^{-4}, as σ_m increases from 0.05 to 0.1. Likewise, for fixed P_o and σ_m, as $\gamma_s/\gamma_{\text{th}}$ increases, the outage performance improves. For instance, for $P_o = 0.5$ and $\sigma_m = 0.05$, the OP decreases from 4.6×10^{-1} to 5.6×10^{-2} as $\gamma_s/\gamma_{\text{th}}$ increases from 10 to 20 dB. Finally, we observe that, for given σ_m and $\gamma_s/\gamma_{\text{th}}$, the OP increases as P_o increases. For example, for $\gamma_s/\gamma_{\text{th}} = 30$ dB and $\sigma_m = 0.1$, the OP increases from 5.24×10^{-8} to 5.24×10^{-5}, as P_o increases from 10^{-3} to 1. This reveals the severity of the joint impact of rain and beam misalignment.

Figure 5 illustrates the throughput as a function of γ_s, for different values of γ_{th} and σ_m, assuming $P_o = 0$,
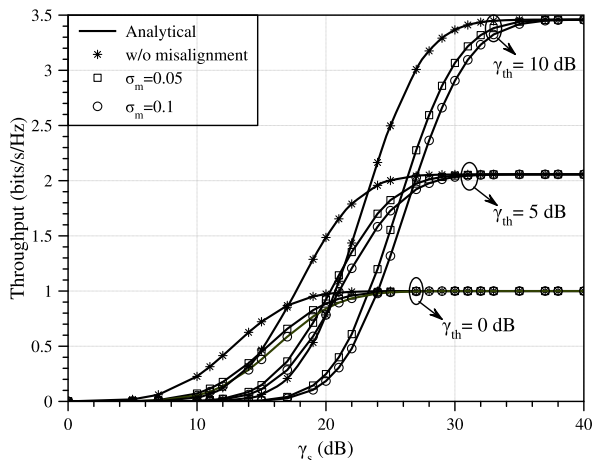
FIGURE 5. OP vs γ_s, for different levels of σ_m, and γ_{th}.
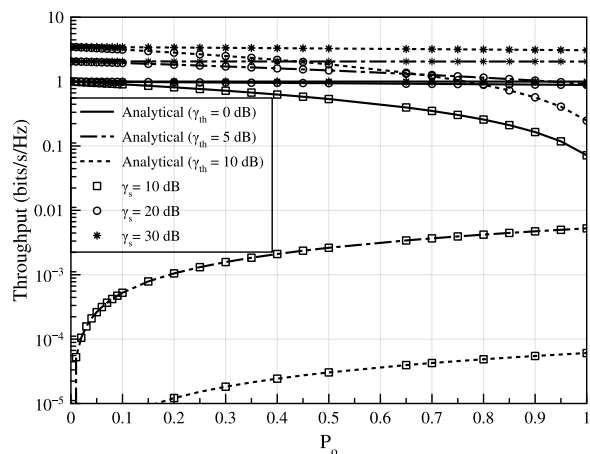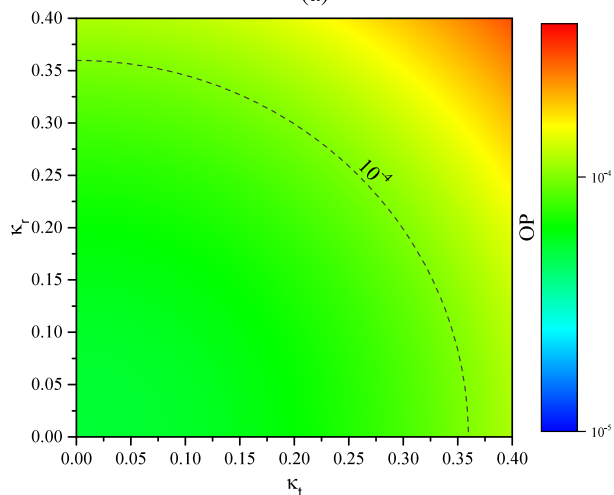

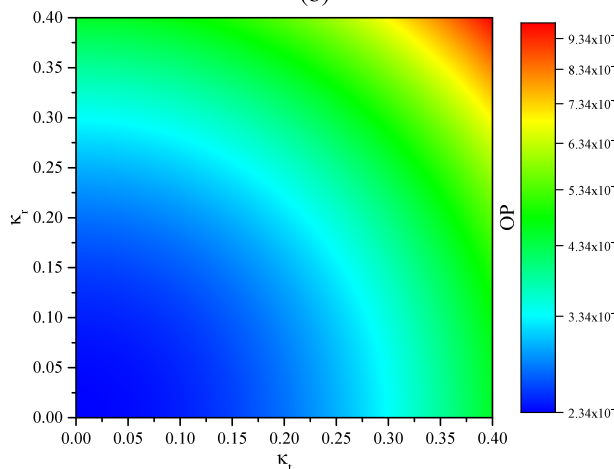**FIGURE 6.** Throughput vs P_o, for different levels of γ_{th}, and γ_s.

$\mu_r = -2.04$, and $\sigma_r = 0.86$. As a benchmark, the throughput in the absence of beam misalignment is also plotted. As expected, for given γ_{th} and σ_m, as γ_s increases, the OP decreases; thus, the throughput increases. For instance, for $\gamma_{th} = 0$ dB and $\sigma_m = 0.05$, the throughput increases from 7.16×10^{-2} to 0.89, as γ_s increases from 10 to 20 dB. Moreover, for a fixed σ_m, the selection of the appropriate transmission scheme that maximizes the achievable throughput depends from the available transmission SNR. For example, for $\sigma_m = 0$, to achieve the maximum possible throughput, a transmission scheme with $\gamma_{th} = 0$ dB should be selected, if the available transmission SNR is lower than 17 dB, whereas, for $\gamma_s \geq 17$ dB and the same σ_m, a transmission scheme with $\gamma_{th} = 5$ dB should be selected. Similarly, for $\sigma_m = 0.05$, a transmission scheme with $\gamma_{th} = 0$ dB should be selected, if $\gamma_s < 20$ dB, while if $\gamma_s > 20$ dB, a transmission scheme with $\gamma_{th} = 5$ dB should be chosen. This example reveals the importance the importance of taking into account the joint impact of beam misalignment and rain as well as the available transmission power, when selecting the appropriate transmission scheme. Finally, we observe that for given γ_s and γ_{th}, as σ_m increases, the throughput decreases. For example, for $\gamma_s = 30$ dB and $\gamma_{th} = 10$ dB,

(a)

(b)

(c)
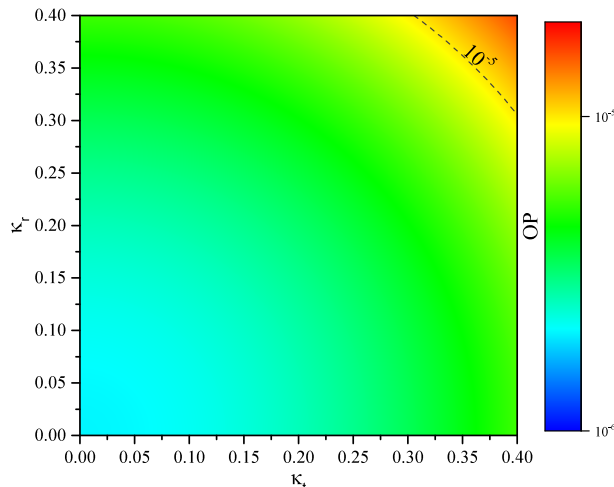
FIGURE 7. OP vs κ_t and κ_r for a) $\sigma_m = 0$, b) $\sigma_m = 0.05$, and c) $\sigma_m = 0.1$.

the throughput decreases from 3.07 to 2.9 bits/s/Hz, as σ_m increases from 0.05 to 0.1. This reveals the importance of accounting the impact of beam misalignment when assessing
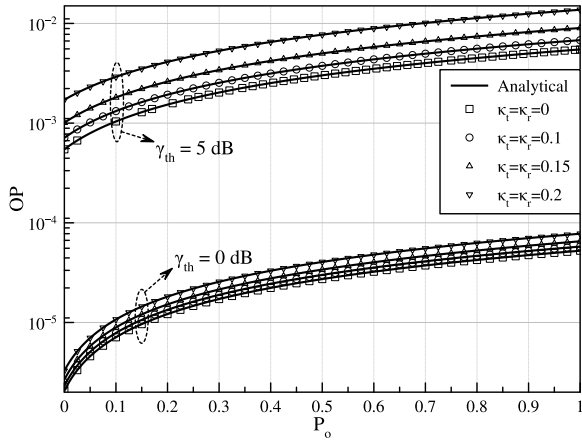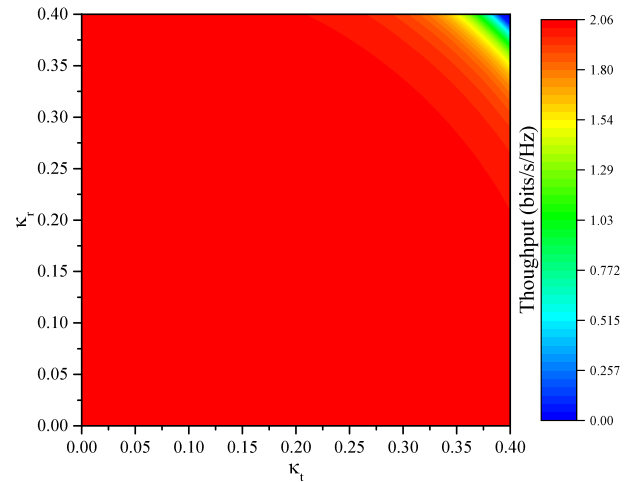
FIGURE 8. OP vs P_o for different values of κ_t, κ_r, and γ_{th}.

the throughput performance of THz wireless systems in the presence of rain.

Figure 6 depicts the throughput as a function of P_o for different values of γ_s and γ_{th}, assuming $\mu_r = -2.04$, $\sigma_r = 0.86$, and $\sigma_m = 0.05$. From this figure, it becomes evident that in the low $\gamma_s/\gamma_{\text{th}}$ regime, where $\gamma_s/\gamma_{\text{th}} \leq \frac{1}{A_o h_t^2}$, i.e., the transmission and reception beams are fully misaligned and thus $F_{h^2|\delta=0}(\gamma_s/\gamma_{\text{th}}) = 1$, the throughput increases, as P_o increases. For instance, for $\gamma_{\text{th}} = \gamma_s = 0$, the throughput increases by about 10 times as P_o changes from 0.2 to 1. On the other hand, for $\gamma_s/\gamma_{\text{th}} > \frac{1}{A_o h_t^2}$, as P_o increases, the throughput decreases.

B. NON-IDEAL RF FRONT-END

Figure 7 illustrates the OP as a function of κ_t and κ_r for different values of σ_m, assuming that $\mu_r = -2.04$, $\sigma_r = 0.86$, $P_o = 0$, $\gamma_s = 30$ dB, and $\gamma_{\text{th}} = 1$ dB. Note that $\kappa_t = \kappa_r = 0$ corresponds to the ideal case in which both the TX and RX are equipped with ideal RF front-end. As expected, for fixed σ_m and κ_t, as κ_r increases, the OP increases. For example, for $\sigma_m = 0$ and $\kappa_t = 0.22$, the OP increases from 2.59×10^{-6} to 6.96×10^{-6}, as κ_r increases from 0.2 to 0.4. Similarly, for given σ_m and κ_r, as κ_t increases, the OP also increases. Likewise, it becomes evident that system A with $\kappa_t = \nu_1$ and $\kappa_r = \nu_2$ achieve the same outage performance as system B with $\kappa_t = \nu_2$ and $\kappa_r = \nu_1$, under the same σ_m. Likewise, from this figure, it becomes apparent that for a fixed σ_m and a constant $\kappa_t + \kappa_r$, the worst outage performance is achieve for $\kappa_t = \kappa_r$. For instance, for $\sigma_m = 0$, and $\kappa_t + \kappa_r = 0.2$, we observe that the OP that is achieved for $\kappa_t = 0$ and $\kappa_r = 0.2$, which is equal to 2.19×10^{-6}, is lower than the OP achieved for $\kappa_t = \kappa_r = 0.1$ (i.e. 2.31×10^{-6}). In addition, we verify that systems with the same $\kappa_t^2 + \kappa_r^2$ achieve the same OP. Finally, for given $\kappa_t^2 + \kappa_r^2$, the OP increases, as σ_m increases. For example, for $\kappa_t^2 + \kappa_r^2 = 0.02$, the OP increases from 2.31×10^{-6} to 2.54×10^{-4}, as σ_m changes from 0 to 0.1. This highlights the importance of accurately modeling the level of beam misalignment.

(a)
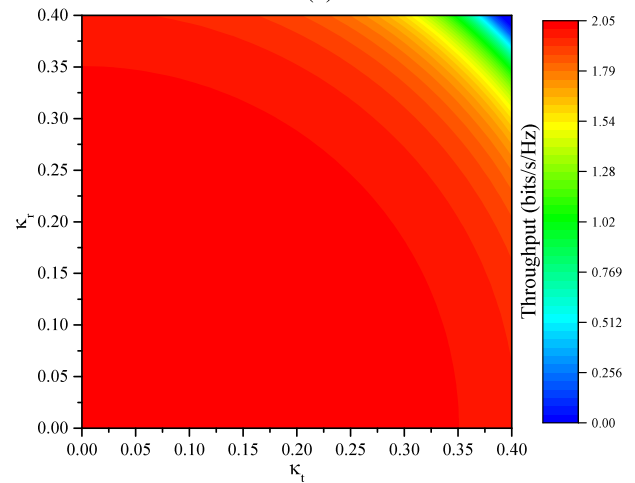
(b)
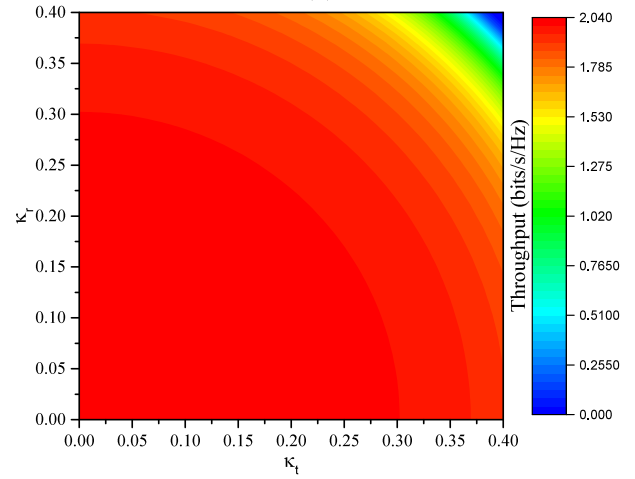
(c)

FIGURE 9. Throughput vs κ_t and κ_r for a) $\sigma_m = 0$, b) $\sigma_m = 0.05$, and c) $\sigma_m = 0.1$.

Figure 8 depicts the OP as a function of P_o for different values of κ_t, κ_r, and γ_{th}, assuming $\mu_r = -2.04$, $\sigma_r = 0.86$, and $\sigma_m = 0.05$. Interestingly, for fixed κ_t, κ_r, and γ_{th}, as P_o
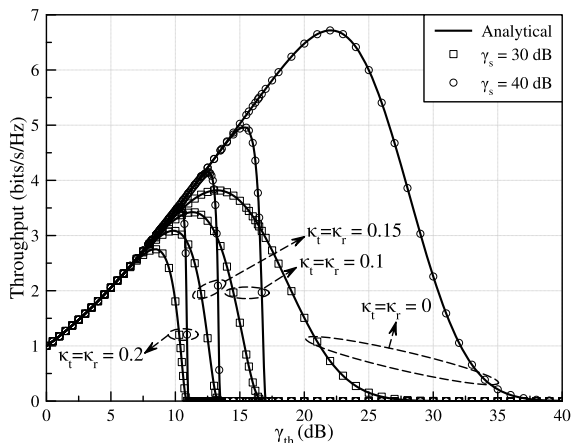
FIGURE 10. Throughput vs γ_{th} for different values of γ_s and $\kappa_t = \kappa_r$.

increases, the OP also increases. Moreover, for given P_o and γ_{th}, as the level of hardware imperfections increases, the OP also increases. For example, for $P_o = 0.5$ and $\gamma_{th} = 5$ dB, the OP increases from 3.8×10^{-3} to 7.7×10^{-3}, as $\kappa_t = \kappa_r$ changes from 0.1 to 0.2. This reveals the importance of accurately modeling the level of hardware imperfections, when assessing the outage performance of wireless THz systems in the presence of misalignment and rain. Finally from this figure, it becomes evident that for a given P_o, as γ_{th} increases, the impact of hardware imperfections on the system's outage performance becomes more detrimental.

Figure 9 presents the throughput as a function of κ_t and κ_r for different values of σ_m, assuming that $\mu_r = -2.04$, $\sigma_r = 0.86$, $P_o = 1$, $\gamma_s = 30$ dB, and $\gamma_{th} = 5$ dB. For given σ_m and κ_t, as κ_r increases, the OP increases; as a result, the achievable throughput decreases. For example, for $\sigma_m = 0$ and $\kappa_t = 0.2$, the achievable throughput decreases from 2.06 to 2.02 bits/s/Hz, as κ_r changes from 0 to 0.4, while, for $\sigma_m = 0.1$, the same κ_t and κ_r change results to an achievable throughput variation from 2.02 to 1.81 bits/s/Hz. This example indicates that as the level of beam misalignment increases, the impact of hardware imperfections on the throughput performance becomes more severe. Moreover, for fixed σ_m and $\kappa_t + \kappa_r$, the minimum achievable throughput is achieved for $\kappa_t = \kappa_r$. Likewise, for a given σ_m, the same throughput is achieve for every κ_t and κ_r combination for which $\kappa_t^2 + \kappa_r^2$ is constant. Finally, for a given $\kappa_t^2 + \kappa_r^2$, the throughput decreases, as σ_m increases.

Figure 10 presents the throughput as a function of γ_{th} for different values of γ_s and $\kappa_t = \kappa_r$, assuming that $\mu_r = -2.04$, $\sigma_r = 0.86$ and $P_o = 1$. From this figure, it becomes evident that an optimal γ_{th} exists that maximizes the achievable throughput. The optimal γ_{th} depends on the transmission SNR γ_s as well as the level of transceivers hardware imperfections. In more detail, for a given γ_s, as the level of hardware imperfections increases, the optimal γ_{th} shifts to lower values. For instance, for $\gamma_s = 40$ dB, as $\kappa_t = \kappa_r$ changes from 0 to 0.2, the optimal γ_{th} shifts from 22 to 10.3 dB. Furthermore, for fixed γ_s and γ_{th}, as $\kappa_t = \kappa_r$

increases, the achievable throughput decreases. For example, for $\gamma_s = 30$ dB and $\gamma_{th} = 30$ dB, the achievable throughput decreases from 3.46 to 1.8 bits/s/Hz, as $\kappa_t = \kappa_r$ increases from 0 to 0.2. Moreover, for a fixed level of transceiver hardware imperfections, the optimal γ_{th} takes higher values, as γ_s increases. Finally, from this figure, we verify that for $\gamma_{th} \geq \frac{1}{\kappa_t^2 + \kappa_r^2}$, the achievable throughput is equal to 0.

VI. CONCLUSION

We investigated the joint effect of rain attenuation, stochastic beam misalignment, and transceiver hardware imperfections in outdoor THz wireless systems. Specifically, we presented a general analytical framework for assessing the OP and achievable throughput for both cases of ideal and non-ideal RF front-end as well as in the presence and the absence of rain. Our results highlighted the degradation due to the joint effect of rain attenuation, misalignment fading, as well as hardware imperfections on the outage and throughput performance of THz wireless systems. Moreover, the existence of an optimal transmission spectral efficiency that depends on the characteristics of the links, the weather conditions, the levels of beam misalignment as well as hardware imperfections at the TX and the RX was revealed. A policy to identify the optimal transmission spectral efficiency that maximizes the achievable throughput was reported. Finally, the importance of accurately characterizing the rain attenuation, misalignment fading, and the levels of harware imperfections when designing and evaluating the outage and throughput performance of outdoor THz wireless systems was documented.

APPENDIX A
PROOF OF LEMMA 1

In the absence of rain, the CDF of h^2 can be obtained as

$$F_{h^2|\delta=0}(x) = \Pr\left(h^2 \leq x \,|\delta = 0\right), \qquad (44)$$

which, with the aid of (2), can be rewritten as

$$F_{h^2|\delta=0}(x) = \Pr\left(h_t^2 \, h_m^2 \leq x \,|\delta = 0\right), \qquad (45)$$

or equivalently

$$F_{h^2|\delta=0}(x) = \Pr\left(h_m^2 \leq \frac{x}{h_t^2} \,|\delta = 0\right). \qquad (46)$$

By applying (10), we obtain (24).

The PDF of h^2 can be obtained as

$$f_{h^2|\delta=0}(x) = \frac{dF_{h^2|\delta=0}(x)}{dx}, \qquad (47)$$

which, by applying (24) can be rewritten as in (23). This concludes the proof.

APPENDIX B
PROOF OF LEMMA 2

The PDF of h^2 can be evaluated as

$$f_{h^2|\delta=1}(x) = f_A\left(\frac{x}{h_t^2}\right), \qquad (48)$$

where $f_A(x)$ is the PDF of

$$A = h_m^2 h_r^2. \qquad (49)$$

Since h_m^2 and h_r^2 are independent RVs, the PDF of A can be obtained as [77]

$$f_A(x) = \int_{\frac{x}{A_o}}^{\infty} \frac{1}{y} f_{h_r^2}(y) f_{h_m^2}\left(\frac{x}{y}\right) dy, \qquad (50)$$

which, by applying (9) and (18) can be written as

$$f_A(x) = \frac{1}{\sqrt{2\pi}\sigma_r} \frac{\xi}{A_o} \left(\frac{x}{A_o}\right)^{\xi-1}$$
$$\times \int_{\frac{x}{A_o}}^{\infty} y^{-\xi-1} \exp\left(-\frac{(\ln(y)-\mu_r)}{2\sigma_r^2}\right) dy. \qquad (51)$$

By setting $z = \ln(y)$, (51) can be rewritten as

$$f_A(x) = \frac{1}{\sqrt{2\pi}\sigma_r} \frac{\xi}{A_o} \left(\frac{x}{A_o}\right)^{\xi-1}$$
$$\times \int_{\ln\left(\frac{x}{A_o}\right)}^{\infty} \exp\left(-\frac{(z-\mu_r)^2}{2\sigma_r^2} - \xi z\right) dz \qquad (52)$$

or equivalent

$$f_A(x) = \frac{1}{\sqrt{2\pi}\sigma_r} \frac{\xi}{A_o} \left(\frac{x}{A_o}\right)^{\xi-1} \exp\left(-\frac{\mu_r^2}{2\sigma_r^2}\right)$$
$$\times \int_{\ln\left(\frac{x}{A_o}\right)}^{\infty} \exp\left(-\frac{z^2 - 2\mu_r z}{2\sigma_r^2} - \xi z\right) dz. \qquad (53)$$

By applying [79, eq.(3.322/1)] in (53), we get

$$f_A(x) = \frac{1}{2} \frac{\xi}{A_o^{\xi}} \exp\left(\frac{\sigma_r^2 \xi^2}{2} - \frac{\xi\mu_r}{\sigma_r}\right) x^{\xi-1}$$
$$\times \operatorname{erfc}\left(\frac{\sigma_r}{\sqrt{2}}\left(\xi - \frac{\mu_r}{\sigma_r^2}\right) + \frac{1}{\sqrt{2}\sigma_r}\ln\left(\frac{x}{A_o}\right)\right). \qquad (54)$$

With the aid of (54), (48),can be written as (25).

The CDF of h^2 can be obtained as

$$F_{h^2|\delta=1}(x) = F_{A|\delta=1}\left(\frac{x}{h_t^2}\right), \qquad (55)$$

where $F_{A|\delta=1}(x)$ is the CDF of A, which can be evaluated as

$$F_{A|\delta=1}(x) = \int_0^x f_A(y) \, dy. \qquad (56)$$

By applying (54) in (56), we obtain

$$F_{A|\delta=1}(x)$$
$$= \frac{1}{2} \frac{\xi}{A_o^{\xi}} \exp\left(\frac{\sigma_r^2 \xi^2}{2} - \frac{\xi\mu_r}{\sigma_r}\right)$$
$$\times \int_0^x y^{\xi-1} \operatorname{erfc}\left(\frac{\sigma_r}{\sqrt{2}}\left(\xi - \frac{\mu_r}{\sigma_r^2}\right) + \frac{1}{\sqrt{2}\sigma_r}\ln\left(\frac{y}{A_o}\right)\right) dy. \qquad (57)$$

By setting

$$z = \frac{\sigma}{\sqrt{2}}\left(\xi - \frac{\mu_r}{\sigma_r^2}\right) - \frac{1}{\sqrt{2}\sigma_r}\ln(A_o) + \frac{1}{\sqrt{2}\sigma_r}\ln(y), \qquad (58)$$

we can rewrite (57) as in (59), as shown at the bottom of the next page. After some algebraic manipulations, (59) can be written as in (60), as shown at the bottom of the next page. By employing [80] and after some algebraic manipulations, (60) can be expressed as in (61), as shown at the bottom of the next page. Finally, by applying (61) in (55), we obtain (26). This concludes the proof.

APPENDIX C
PROOF OF PROPOSITION 2
The OP is defined as

$$P_{\text{out}}(\gamma_{\text{th}}) = \Pr(\gamma \le \gamma_{\text{th}}), \qquad (62)$$

which, by applying (31) can be equivalently written as

$$P_{\text{out}}(\gamma_{\text{th}}) = \Pr\left(h^2\left(1 - \gamma_{\text{th}}\left(\kappa_t^2 + \kappa_r^2\right)\right) \le \gamma_{\text{th}} N_o\right). \qquad (63)$$

For $\gamma_{\text{th}}(\kappa_t^2 + \kappa_r^2) \ge 1$, the condition $1 - \gamma_{\text{th}}(\kappa_t^2 + \kappa_r^2) \le 0 \le \gamma_{\text{th}} N_o$ is always valid. Thus,

$$P_{\text{out}}(\gamma_{\text{th}}) = 1, \text{ for } \gamma_{\text{th}} \ge \frac{1}{\kappa_t^2 + \kappa_r^2}. \qquad (64)$$

On the other hand, for $\gamma_{\text{th}} < \frac{1}{\kappa_t^2 + \kappa_r^2}$, (63) can be rewritten as

$$P_{\text{out}}(\gamma_{\text{th}}) = \Pr\left(h^2 \le \frac{1}{\left(1 - \gamma_{\text{th}}\left(\kappa_t^2 + \kappa_r^2\right)\right)}\gamma_{\text{th}} N_o\right),$$
$$\text{for } \gamma_{\text{th}} < \frac{1}{\kappa_t^2 + \kappa_r^2}. \qquad (65)$$

or

$$P_{\text{out}}(\gamma_{\text{th}}) = F_h^2\left(\frac{1}{\left(1 - \gamma_{\text{th}}\left(\kappa_t^2 + \kappa_r^2\right)\right)}\gamma_{\text{th}} N_o\right),$$
$$\text{for } \gamma_{\text{th}} < \frac{1}{\kappa_t^2 + \kappa_r^2}. \qquad (66)$$

By combining (64) and (66), we obtain (33). This concludes the proof.

APPENDIX D
PROOF OF PROPOSITION 3
By applying (33) to (39), the achievable throughput can be rewritten as

$$D(\gamma_{\text{th}})$$
$$= \begin{cases} \log_2(1 + \gamma_{\text{th}})\left(1 - (1 - P_o) F_{h^2|\delta=0}(\zeta\gamma_{\text{th}}) \right. \\ \left. -P_o F_{h^2|\delta=1}(\zeta\gamma_{\text{th}})\right), & \text{for } \gamma_{\text{th}} < \frac{1}{\kappa_t^2 + \kappa_r^2} \\ 0, & \text{for } \gamma_{\text{th}} \ge \frac{1}{\kappa_t^2 + \kappa_r^2}, \end{cases} \qquad (67)$$

where

$$\zeta = \frac{1}{\tilde{\gamma}} \frac{1}{1 - \gamma_{\text{th}}\left(\kappa_t^2 + \kappa_r^2\right)}. \qquad (68)$$

From (67), for $\gamma_{\text{th}} < \frac{1}{\kappa_t^2 + \kappa_r^2}$, it is evident that in the low-γ_{th} regime, where $F_{h^2|\delta=0}(\zeta\gamma_{\text{th}})$ and $F_{h^2|\delta=1}(\zeta\gamma_{\text{th}})$ tent to 0, the achievable throughput is mainly affected by

$$f_1(\gamma_{\text{th}}) = \log_2(1 + \gamma_{\text{th}}), \qquad (69)$$

which is an increasing function. On the other hand, in the high-γ_{th} regime, where $F_{h^2|\delta=0}(\zeta\gamma_{\text{th}})$ and $F_{h^2|\delta=1}(\zeta\gamma_{\text{th}})$ tent to 1, the achievable throughput is mainly affected by

$$f_2(\gamma_{\text{th}}) = 1 - (1 - P_o)F_{h^2|\delta=0}(\zeta\gamma_{\text{th}})$$
$$-P_oF_{h^2|\delta=1}(\zeta\gamma_{\text{th}}), \qquad (70)$$

which is a decreasing function. Since the achievable throughput is an continuous function of γ_{th}, the aforementioned observations indicate that (67) is a concave function. In other words, there exists γ_{th}^o that maximizes the achievable throughput. Apparently, for the γ_{th}^o, the following inequality is valid:

$$\gamma_{\text{th}}^o < \frac{1}{\kappa_t^2 + \kappa_r^2}. \qquad (71)$$

For $\gamma_{\text{th}} < \frac{1}{\kappa_t^2 + \kappa_r^2}$, the first derivative of (67) can be obtained as in (72), as shown at the bottom of the page, or equivalently as in (73), as shown at the bottom of the page. Notice that

$$\frac{dF_{h^2|\delta=0}(\zeta\gamma_{\text{th}})}{d(\zeta\gamma_{\text{th}})} = f_{h^2|\delta=0}(\zeta\gamma_{\text{th}}) \qquad (74)$$

and

$$\frac{d(\zeta\gamma_{\text{th}})}{d\gamma_{\text{th}}} = \zeta + \gamma_{\text{th}}\frac{d\zeta}{d\gamma_{\text{th}}}, \qquad (75)$$

with

$$\frac{d\zeta}{d\gamma_{\text{th}}} = \frac{\kappa_t^2 + \kappa_r^2}{\tilde{\gamma}\left(1 - \left(\kappa_t^2 + \kappa_r^2\right)\gamma_{\text{th}}\right)^2}. \qquad (76)$$

By applying (76) to (75), we get

$$\frac{d(\zeta\gamma_{\text{th}})}{d\gamma_{\text{th}}} = \zeta + \gamma_{\text{th}}\frac{\kappa_t^2 + \kappa_r^2}{\tilde{\gamma}\left(1 - \left(\kappa_t^2 + \kappa_r^2\right)\gamma_{\text{th}}\right)^2}. \qquad (77)$$

$$F_{A|\delta=1}(x) = \frac{1}{2}\frac{\xi}{A_o^\xi}\exp\left(\frac{\sigma_r^2\xi^2}{2} - \frac{\xi\mu_r}{\sigma_r}\right)$$
$$\times \int_{-\infty}^{\frac{\sigma_r}{\sqrt{2}}\left(\xi - \frac{\mu_r}{\sigma_r^2}\right) - \frac{1}{\sqrt{2}\sigma_r}\ln(A_o) + \frac{1}{\sqrt{2}\sigma_r}\ln(x)}\left(\exp\left(\frac{z - \left(\frac{\sigma_r}{\sqrt{2}}\left(\xi - \frac{\mu_r}{\sigma_r^2}\right) - \frac{1}{\sqrt{2}\sigma_r}\ln(A_o)\right)}{\frac{1}{\sqrt{2}\sigma_r}}\right)\right)^\xi \text{erfc}(z)\, dz \quad (59)$$

$$F_{A|\delta=1}(x) = \frac{\sigma_r\sqrt{2}}{2}\frac{\xi}{A_o^\xi}\exp\left(-\frac{\mu_r^2}{2\sigma_r^2} + \frac{\sigma_r^2}{2}\left(\xi - \frac{\mu_r}{\sigma_r^2}\right)^2 - \sigma_r^2\xi\left(\xi - \frac{\mu_r}{\sigma_r^2}\right) + \xi\ln(A_o)\right)$$
$$\times \int_{-\infty}^{\frac{\sigma_r}{\sqrt{2}}\left(\xi - \frac{\mu_r}{\sigma_r^2}\right) - \frac{1}{\sqrt{2}\sigma_r}\ln(A_o) + \frac{1}{\sqrt{2}\sigma_r}\ln(x)}\exp\left(\sigma_r\sqrt{2}\xi z\right)\text{erfc}(z)\, dz \quad (60)$$

$$F_{A|\delta=1}(x) = \frac{1}{2A_o^\xi}\exp\left(\xi\ln(A_o) - \frac{\sigma_r^2\xi^2}{2}\right)$$
$$\times \left(\exp\left(\frac{\sigma_r^2\xi^2}{2}\right)\text{erfc}\left(\frac{\sqrt{2}}{2\sigma_r}\left(\mu_r + \ln\left(\frac{x}{A_o}\right)\right)\right)\right.$$
$$\left. + \exp\left(\sigma_r^2\xi\left(\xi - \frac{\mu_r}{\sigma_r^2}\right)\right)\text{erfc}\left(\frac{\sqrt{2}\sigma_r}{2}\left(\xi - \frac{\mu_r}{\sigma_r^2}\right) + \frac{1}{\sqrt{2}\sigma_r}\ln\left(\frac{x}{A_o}\right)\right)\right) \quad (61)$$

$$\frac{dD(\gamma_{\text{th}})}{d\gamma_{\text{th}}} = \frac{1}{\ln(2)}\frac{1}{1 + \gamma_{\text{th}}}\left(1 - (1 - P_o)F_{h^2|\delta=0}(\zeta\gamma_{\text{th}}) - P_oF_{h^2|\delta=1}(\zeta\gamma_{\text{th}})\right)$$
$$- \log_2(1 + \gamma_{\text{th}})\left((1 - P_o)\frac{dF_{h^2|\delta=0}(\zeta\gamma_{\text{th}})}{d\gamma_{\text{th}}} + P_o\frac{dF_{h^2|\delta=1}(\zeta\gamma_{\text{th}})}{d\gamma_{\text{th}}}\right) \quad (72)$$

$$\frac{dD(\gamma_{\text{th}})}{d\gamma_{\text{th}}} = \frac{1}{\ln(2)}\frac{1}{1 + \gamma_{\text{th}}}\left(1 - (1 - P_o)F_{h^2|\delta=0}(\zeta\gamma_{\text{th}}) - P_oF_{h^2|\delta=1}(\zeta\gamma_{\text{th}})\right)$$
$$- \log_2(1 + \gamma_{\text{th}})\left((1 - P_o)\frac{dF_{h^2|\delta=0}(\zeta\gamma_{\text{th}})}{d(\zeta\gamma_{\text{th}})}\frac{d(\zeta\gamma_{\text{th}})}{d\gamma_{\text{th}}} + P_o\frac{dF_{h^2|\delta=1}(\zeta\gamma_{\text{th}})}{d(\zeta\gamma_{\text{th}})}\frac{d(\zeta\gamma_{\text{th}})}{d\gamma_{\text{th}}}\right) \quad (73)$$

$$\frac{\mathrm{d}D\left(\gamma_{\mathrm{th}}\right)}{\mathrm{d}\gamma_{\mathrm{th}}} = \frac{1}{\ln(2)}\frac{1}{1+\gamma_{\mathrm{th}}}\left(1-(1-P_o)\,F_{h^2|\delta=0}\left(\zeta\gamma_{\mathrm{th}}\right)-P_o F_{h^2|\delta=1}\left(\zeta\gamma_{\mathrm{th}}\right)\right)$$
$$-\log_2\left(1+\gamma_{\mathrm{th}}\right)\left(\zeta+\gamma_{\mathrm{th}}\frac{\kappa_t^2+\kappa_r^2}{\tilde{\gamma}\left(1-\left(\kappa_t^2+\kappa_r^2\right)\gamma_{\mathrm{th}}\right)^2}\right)\left((1-P_o)\,f_{h^2|\delta=0}\left(\zeta\gamma_{\mathrm{th}}\right)+P_o f_{h^2|\delta=1}\left(\zeta\gamma_{\mathrm{th}}\right)\right) \quad (78)$$

$$\frac{\mathrm{d}D\left(\gamma_{\mathrm{th}}\right)}{\mathrm{d}\gamma_{\mathrm{th}}} = \frac{1}{\ln(2)}\frac{1}{1+\gamma_{\mathrm{th}}}P_{\mathrm{out}}\left(\gamma_{\mathrm{th}}\right)-\log_2\left(1+\gamma_{\mathrm{th}}\right)\left(\zeta+\gamma_{\mathrm{th}}\frac{\kappa_t^2+\kappa_r^2}{\tilde{\gamma}\left(1-\left(\kappa_t^2+\kappa_r^2\right)\gamma_{\mathrm{th}}\right)^2}\right)f_{h^2}\left(\zeta\gamma_{\mathrm{th}}\right) \quad (79)$$

$$\frac{\mathrm{d}D\left(\gamma_{\mathrm{th}}\right)}{\mathrm{d}\gamma_{\mathrm{th}}} = \frac{1}{\ln(2)}\frac{1}{1+\gamma_{\mathrm{th}}}P_{\mathrm{out}}\left(\gamma_{\mathrm{th}}\right)-\log_2\left(1+\gamma_{\mathrm{th}}\right)\left(\frac{1}{\tilde{\gamma}\left(1-\left(\kappa_t^2+\kappa_r^2\right)\gamma_{\mathrm{th}}\right)}+\gamma_{\mathrm{th}}\frac{\kappa_t^2+\kappa_r^2}{\tilde{\gamma}\left(1-\left(\kappa_t^2+\kappa_r^2\right)\gamma_{\mathrm{th}}\right)^2}\right)$$
$$\times f_{h^2}\left(\frac{\gamma_{\mathrm{th}}}{\tilde{\gamma}\left(1-\left(\kappa_t^2+\kappa_r^2\right)\gamma_{\mathrm{th}}\right)}\right) \quad (80)$$

By substituting (74) and (77) into (73), we obtain (78), as shown at the top of the page. By applying (28) and (27), (78) can be equivalently rewritten as in (79), as shown at the top of the page. Next, with the aid of (68), (79) can be expressed as in (80), as shown at the top of the page.

The maximum throughput is achieved for the SNR threshold, γ_{th}^o for which

$$\left.\frac{\mathrm{d}D\left(\gamma_{\mathrm{th}}\right)}{\mathrm{d}\gamma_{\mathrm{th}}}\right|_{\gamma_{\mathrm{th}}=\gamma_{\mathrm{th}}^o} = 0. \quad (81)$$

By applying (81) into (80), we obtain (40). This concludes the proof.

REFERENCES

[1] M. Matthaiou, O. Yurduseven, H. Q. Ngo, D. Morales-Jimenez, S. L. Cotton, and V. F. Fusco, "The road to 6G: Ten physical layer challenges for communications engineers," *IEEE Commun. Mag.*, vol. 59, no. 1, pp. 64–69, Jan. 2021.

[2] A.-A. A. Boulogeorgos, A. Alexiou, T. Merkle, C. Schubert, R. Elschner, A. Katsiotis, P. Stavrianos, D. Kritharidis, P. K. Chartsias, J. Kokkoniemi, M. Juntti, J. Lehtomäki, A. Teixeirá, and F. Rodrigues, "Terahertz technologies to deliver optical network quality of experience in wireless systems beyond 5G," *IEEE Commun. Mag.*, vol. 56, no. 6, pp. 144–151, Jun. 2018.

[3] A.-A. A. Boulogeorgos, A. Alexiou, D. Kritharidis, A. Katsiotis, G. Ntouni, J. Kokkoniemi, J. Lethtomaki, M. Juntti, D. Yankova, A. Mokhtar, J.-C. Point, J. Machodo, R. Elschner, C. Schubert, T. Merkle, R. Ferreira, F. Rodrigues, and J. Lima, "Wireless terahertz system architectures for networks beyond 5G," Terranova Consortium, Chennai, India, White Paper 1.0, Jul. 2018.

[4] A.-A.-A. Boulogeorgos, E. N. Papasotiriou, and A. Alexiou, "Analytical performance assessment of THz wireless systems," *IEEE Access*, vol. 7, pp. 11436–11453, 2019.

[5] A.-A.-A. Boulogeorgos and A. Alexiou, "Error analysis of mixed THz-RF wireless systems," *IEEE Commun. Lett.*, vol. 24, no. 2, pp. 277–281, Feb. 2020.

[6] C. Castro, R. Elschner, T. Merkle, C. Schubert, and R. Freund, "Experimental demonstrations of high-capacity THz-wireless transmission systems for beyond 5G," *IEEE Commun. Mag.*, vol. 58, no. 11, pp. 41–47, Nov. 2020.

[7] Z. Zhang, Y. Xiao, Z. Ma, M. Xiao, Z. Ding, X. Lei, G. K. Karagiannidis, and P. Fan, "6G wireless networks: Vision, requirements, architecture, and key technologies," *IEEE Veh. Technol. Mag.*, vol. 14, no. 3, pp. 28–41, Sep. 2019.

[8] J. M. Jornet and I. F. Akyildiz, "Channel modeling and capacity analysis for electromagnetic wireless nanonetworks in the terahertz band," *IEEE Trans. Wireless Commun.*, vol. 10, no. 10, pp. 3211–3221, Oct. 2011.

[9] J. Kokkoniemi, J. Lehtomäki, and M. Juntti, "Frequency domain scattering loss in THz band," in *Proc. Global Symp. Millim.-Waves (GSMM)*, Montreal, QC, Canada, May 2015, pp. 1–3.

[10] E. N. Papasotiriou, J. Kokkoniemi, A.-A. A. Boulogeorgos, J. Lehtomäki, A. Alexiou, and M. Juntti, "A new look to 275 to 400 GHz band: Channel model and performance evaluation," in *Proc. IEEE Int. Symp. Pers., Indoor Mobile Radio Commun. (PIMRC)*, Bolonia, Italy, Sep. 2018, pp. 1–5.

[11] A.-A. A. Boulogeorgos, E. N. Papasotiriou, J. Kokkoniemi, J. Lehtomäki, A. Alexiou, and M. Juntti, "Performance evaluation of THz wireless systems operating in 275–400 GHz band," in *Proc. IEEE Veh. Technol. Conf. (VTC)*, Jun. 2018, pp. 1–5.

[12] A.-A.-A. Boulogeorgos, E. N. Papasotiriou, and A. Alexiou, "A distance and bandwidth dependent adaptive modulation scheme for THz communications," in *Proc. IEEE 19th Int. Workshop Signal Process. Adv. Wireless Commun. (SPAWC)*, Kalamata, Greece, Jun. 2018, pp. 1–5.

[13] J. Kokkoniemi, J. Lehtomäki, and M. Juntti, "Simplified molecular absorption loss model for 275–400 gigahertz frequency band," in *Proc. 12th Eur. Conf. Antennas Propag. (EuCAP)*, London, U.K., Apr. 2018, pp. 1–5.

[14] I. F. Akyildiz, J. M. Jornet, and C. Han, "Terahertz band: Next frontier for wireless communications," *Phys. Commun.*, vol. 12, pp. 16–32, Sep. 2014.

[15] A.-A.-A. Boulogeorgos, S. K. Goudos, and A. Alexiou, "Users association in ultra dense THz networks," in *Proc. IEEE 19th Int. Workshop Signal Process. Adv. Wireless Commun. (SPAWC)*, Kalamata, Greece, Jun. 2018, pp. 1–5.

[16] M. Xiao, S. Mumtaz, Y. Huang, L. Dai, Y. Li, M. Matthaiou, G. K. Karagiannidis, E. Bjornson, K. Yang, I. Chih-Lin, and A. Ghosh, "Millimeter wave communications for future mobile networks," *IEEE J. Sel. Areas Commun.*, vol. 35, no. 9, pp. 1909–1935, Sep. 2017.

[17] J. Kokkoniemi, A.-A.-A. Boulogeorgos, M. Aminu, J. Lehtomäki, A. Alexiou, and M. Juntti, "Impact of beam misalignment on THz wireless systems," *Nano Commun. Netw.*, vol. 24, May 2020, Art. no. 100302.

[18] A.-A.-A. Boulogeorgos, E. N. Papasotiriou, and A. Alexiou, "Analytical performance evaluation of THz wireless fiber extenders," in *Proc. IEEE 30th Annu. Int. Symp. Pers., Indoor Mobile Radio Commun. (PIMRC)*, Sep. 2019, pp. 1–6.

[19] A.-A. A. Boulogeorgos and A. Alexiou, "Antenna misalignment and blockage in THz communications," in *Next Generation Wireless Terahertz Communication Networks*. Boca Raton, FL, USA: CRC Press, Jun. 2021, pp. 213–247.

[20] S. Priebe, M. Jacob, and T. Kurner, "The impact of antenna directivities on THz indoor channel characteristics," in *Proc. 6th Eur. Conf. Antennas Propag. (EUCAP)*, Mar. 2012, pp. 478–482.

[21] S. Priebe, M. Jacob, and T. Kurner, "Affection of THz indoor communication links by antenna misalignment," in *Proc. 6th Eur. Conf. Antennas Propag. (EUCAP)*, Mar. 2012, pp. 483–487.

[22] A. R. Ekti, A. Boyaci, A. Alparslan, A. Ünal, S. Yarkan, A. Gorcin, H. Arslan, and M. Uysal, "Statistical modeling of propagation channels for terahertz band," in *Proc. IEEE Conf. Standards Commun. Netw. (CSCN)*, Helsinki, Finland, Sep. 2017, pp. 275–280.

[23] F. Sheikh, Y. Zantah, M. Al-Hasan, and T. Kaiser, "Novel aspects of horn-antenna beam misalignment at THz frequencies," in *Proc. IEEE-APS Topical Conf. Antennas Propag. Wireless Commun. (APWC)*, Aug. 2021, p. 65.

[24] F. Sheikh, Y. Zantah, M. Al-Hasan, I. Mabrouk, N. Zarifeh, and T. Kaiser, "Horn antenna misalignments at 100, 300, 400, and 500 GHz in close proximity communications," in *Proc. IEEE Int. Symp. Antennas Propag. USNC-URSI Radio Sci. Meeting (APS/URSI)*, Dec. 2021, pp. 449–450.

[25] E. N. Papasotiriou, A.-A.-A. Boulogeorgos, and A. Alexiou, "Performance analysis of THz wireless systems in the presence of antenna misalignment and phase noise," *IEEE Commun. Lett.*, vol. 24, no. 6, pp. 1211–1215, Jun. 2020.

[26] O. S. Badarneh, "Performance analysis of terahertz communications in random fog conditions with misalignment," *IEEE Wireless Commun. Lett.*, vol. 11, no. 5, pp. 962–966, May 2022.

[27] L. Bao, H. Zhao, G. Zheng, and W. Zhao, "The influence of turbulence scintillation on the BER of THz wireless communication," in *Proceedings of the 2012 International Conference on Information Technology and Software Engineering* (Lecture Notes in Electrical Engineering). Berlin, Germany: Springer, Nov. 2012, pp. 167–174.

[28] J. F. Federici, J. Ma, and L. Moeller, "Review of weather impact on outdoor terahertz wireless communication links," *Nano Commun. Netw.*, vol. 10, pp. 13–26, Dec. 2016.

[29] M. Uysal, J. Li, and M. Yu, "Error rate performance analysis of coded free-space optical links over gamma-gamma atmospheric turbulence channels," *IEEE Trans. Wireless Commun.*, vol. 5, no. 6, pp. 1229–1233, Jun. 2006.

[30] T. Schneider, A. Wiatrek, S. Preußler, M. Grigat, and R.-P. Braun, "Link budget analysis for terahertz fixed wireless links," *IEEE Trans. THz Sci. Technol.*, vol. 2, no. 2, pp. 250–256, Mar. 2012.

[31] K. Su, L. Moeller, R. B. Barat, and J. F. Federici, "Experimental comparison of performance degradation from terahertz and infrared wireless links in fog," *J. Opt. Soc. Amer. A, Opt. Image Sci.*, vol. 29, no. 2, p. 179, Jan. 2012.

[32] Y. Yang, M. Mandehgar, and D. R. Grischkowsky, "Broadband THz signals propagate through dense fog," *IEEE Photon. Technol. Lett.*, vol. 27, no. 4, pp. 383–386, Feb. 15, 2015.

[33] J. Ma, F. Vorrius, L. Lamb, L. Moeller, and J. F. Federici, "Experimental comparison of terahertz and infrared signaling in laboratory-controlled rain," *J. Infr., Millim., THz Waves*, vol. 36, no. 9, pp. 856–865, Jun. 2015.

[34] M. E. Shawon, M. Z. Chowdhury, M. B. Hossen, M. F. Ahmed, and Y. M. Jang, "Rain attenuation characterization for 6G terahertz wireless communication," in *Proc. Int. Conf. Artif. Intell. Inf. Commun. (ICAIIC)*, Apr. 2021, pp. 416–420.

[35] R. Wang, Y. Mei, X. Meng, and J. Ma, "Secrecy performance of terahertz wireless links in rain and snow," *Nano Commun. Netw.*, vol. 28, Jun. 2021, Art. no. 100350.

[36] J. Ma, L. Moeller, and J. F. Federici, "Experimental comparison of terahertz and infrared signaling in controlled atmospheric turbulence," *J. Infr., Millim., THz Waves*, vol. 36, no. 2, pp. 130–143, Nov. 2014.

[37] L. Cang, H.-K. Zhao, and G.-X. Zheng, "The impact of atmospheric turbulence on terahertz communication," *IEEE Access*, vol. 7, pp. 88685–88692, 2019.

[38] M. Taherkhani, Z. G. Kashani, and R. A. Sadeghzadeh, "On the performance of THz wireless LOS links through random turbulence channels," *Nano Commun. Netw.*, vol. 23, Feb. 2020, Art. no. 100282.

[39] A.-A. Boulogeorgos, N. D. Chatzidiamantis, H. Sandalidis, A. Alexiou, and M. D. Renzo, "Cascaded composite turbulence and misalignment: Statistical characterization and applications to reconfigurable intelligent surface-empowered wireless systems," *IEEE Trans. Veh. Technol.*, vol. 71, no. 4, pp. 3821–3836, Apr. 2022.

[40] M. Taherkhani, Z. G. Kashani, and R. Sadeghzadeh, "Average bit error rate and channel capacity of terahertz wireless line-of-sight links with pointing errors under combined effects of turbulence and snow," *Appl. Opt.*, vol. 59, no. 33, p. 10345, Nov. 2020.

[41] X. Yang, M. Matthaiou, J. Yang, C.-K. Wen, F. Gao, and S. Jin, "Hardware-constrained millimeter-wave systems for 5G: Challenges, opportunities, and solutions," *IEEE Commun. Mag.*, vol. 57, no. 1, pp. 44–50, Jan. 2019.

[42] T. Schenk, *RF Imperfections in High-Rate Wireless Systems*. Amsterdam, The Netherlands: Springer, 2008.

[43] T. Mao, Q. Wang, and Z. Wang, "Receiver design for the low-cost terahertz communication system with hardware impairment," in *Proc. IEEE Int. Conf. Commun. (ICC)*, Dublin, Ireland, Jun. 2020, pp. 1–5.

[44] P. Rykaczewski, M. Valkama, and M. Renfors, "On the connection of I/Q imbalance and channel equalization in direct-conversion transceivers," *IEEE Trans. Veh. Technol.*, vol. 57, no. 3, pp. 1630–1636, May 2008.

[45] A. Gokceoglu, Y. Zou, M. Valkama, and P. C. Sofotasios, "Multi-channel energy detection under phase noise: Analysis and mitigation," *Mobile Netw. Appl.*, vol. 19, no. 4, pp. 473–486, May 2014.

[46] L. Anttila, M. Valkama, and M. Renfors, "Frequency-selective I/Q mismatch calibration of wideband direct-conversion transmitters," *IEEE Trans. Circuits Syst. II, Exp. Briefs*, vol. 55, no. 4, pp. 359–363, Apr. 2008.

[47] A.-A. A. Boulogeorgos, "Interference mitigation techniques in modern wireless communication systems," Ph.D. dissertation, Aristotle Univ. Thessaloniki, Thessaloniki, Greece, Sep. 2016.

[48] A.-A. A. Boulogeorgos, N. D. Chatzidiamantis, and G. K. Karagiannidis, "Energy detection spectrum sensing under RF imperfections," *IEEE Trans. Commun.*, vol. 64, no. 7, pp. 2754–2766, Jul. 2016.

[49] A.-A. A. Boulogeorgos and G. K. Karagiannidis, "Energy detection in full-duplex systems with residual RF impairments over fading channels," *IEEE Wireless Commun. Lett.*, vol. 7, no. 2, pp. 246–249, Apr. 2018.

[50] A.-A. A. Boulogeorgos, V. M. Kapinas, R. Schober, and G. K. Karagiannidis, "I/Q-imbalance self-interference coordination," *IEEE Trans. Wireless Commun.*, vol. 15, no. 6, pp. 4157–4170, Jun. 2016.

[51] E. Björnson, M. Matthaiou, and M. Debbah, "A new look at dual-hop relaying: Performance limits with hardware impairments," *IEEE Trans. Commun.*, vol. 61, no. 11, pp. 4512–4525, Nov. 2013.

[52] E. Björnson, M. Matthaiou, and M. Debbah, "Massive MIMO systems with hardware-constrained base stations," in *Proc. IEEE Int. Conf. Acoust., Speech Signal Process. (ICASSP)*, Florence, Italy, May 2014, pp. 3142–3146.

[53] E. Soleimani-Nasab, M. Matthaiou, M. Ardebilipour, and G. K. Karagiannidis, "Two-way AF relaying in the presence of co-channel interference," *IEEE Trans. Commun.*, vol. 61, no. 8, pp. 3156–3169, Aug. 2013.

[54] S. Koenig, D. Lopez-Diaz, J. Antes, F. Boes, R. Henneberger, A. Leuther, A. Tessmann, R. Schmogrow, D. Hillerkuss, R. Palmer, T. Zwick, C. Koos, W. Freude, O. Ambacher, J. Leuthold, and I. Kallfass, "Wireless sub-THz communication system with high data rate," *Nature Photon.*, vol. 7, no. 12, pp. 977–981, Dec. 2013.

[55] I. Kallfass, I. Dan, S. Rey, P. Harati, J. Antes, A. Tessmann, S. Wagner, M. Kuri, R. Weber, H. Massler, A. Leuther, T. Merkle, and T. Kürner, "Towards MMIC-based 300 GHz indoor wireless communication systems," *IEICE Trans. Electron.*, vol. E98.C, no. 12, pp. 1081–1090, 2015.

[56] T. Mao, Q. Wang, and Z. Wang, "Spatial modulation for terahertz communication systems with hardware impairments," *IEEE Trans. Veh. Technol.*, vol. 69, no. 4, pp. 4553–4557, Apr. 2020.

[57] G. Brussaard and P. A. Watson, *Atmospheric Modelling and Millimetre Wave Propagation*. Amsterdam, The Netherlands: Springer, Dec. 1994.

[58] *Characteristics of Precipitation for Propagation Modelling*, document ITU-R P.837-5, Geneva, Switzerland, 2007.

[59] M. Wenk, *MIMO-OFDM Testbed: Challenges, Implementations, and Measurement Results* (Series in Microelectronics). Zürich, Switzerland: ETH, 2010.

[60] A.-A. A. Boulogeorgos and A. Alexiou, "Analytical performance evaluation of beamforming under transceivers hardware imperfections," in *Proc. IEEE Wireless Commun. Netw. Conf. (WCNC)*, Marrakesh, Morocco, Apr. 2019, pp. 1–7.

[61] M. Mokhtar, A. Gomaa, and N. Al-Dhahir, "OFDM AF relaying under I/Q imbalance: Performance analysis and baseband compensation," *IEEE Trans. Commun.*, vol. 61, no. 4, pp. 1304–1313, Apr. 2013.

[62] T. L. Jensen and T. Larsen, "Robust computation of error vector magnitude for wireless standards," *IEEE Trans. Commun.*, vol. 61, no. 2, pp. 648–657, Feb. 2013.

[63] A.-A.-A. Boulogeorgos and A. Alexiou, "How much do hardware imperfections affect the performance of reconfigurable intelligent surface-assisted systems?" *IEEE Open J. Commun. Soc.*, vol. 1, pp. 1185–1195, 2020.

[64] E. A. L. S. Rothman, "The HITRAN 2008 molecular spectroscopic database," *J. Quant. Spectrosc. Radiat. Transf.*, vol. 110, nos. 9–10, pp. 533–572, Jun. 2009.

[65] H. Elayan, R. M. Shubair, J. M. Jornet, and P. Johari, "Terahertz channel model and link budget analysis for intrabody nanoscale communication," *IEEE Trans. Nanobiosci.*, vol. 16, no. 6, pp. 491–503, Sep. 2017.

[66] J. M. Jornet and I. F. Akyildiz, "Channel capacity of electromagnetic nanonetworks in the terahertz band," in *Proc. IEEE Int. Conf. Commun. (ICC)*, Cape Town, South Africa, May 2010, pp. 1–6.

[67] J. Kokkoniemi, J. Lehtomaki, and M. Juntti, "Simplified molecular absorption loss model for 275–400 gigahertz frequency band," in *Proc. 12th Eur. Conf. Antennas Propag. (EuCAP)*. London, U.K.: Institution of Engineering and Technology, Apr. 2018, pp. 1–5.

[68] K. Tsujimura, K. Umebayashi, J. Kokkoniemi, J. Lehtomaki, and Y. Suzuki, "A causal channel model for the terahertz band," *IEEE Trans. THz Sci. Technol.*, vol. 8, no. 1, pp. 52–62, Jan. 2018.

[69] J. Kokkoniemi, J. M. Jornet, V. Petrov, Y. Koucheryavy, and M. Juntti, "Channel modeling and performance analysis of airplane-satellite terahertz band communications," *IEEE Trans. Veh. Technol.*, vol. 70, no. 3, pp. 2047–2061, Mar. 2021.

[70] C. A. Balanis, *Modern Antenna Handbook*. New York, NY, USA: Wiley, 2008.

[71] *Tropospheric Attenuation Time Series Synthesis*, document ITU-R P.1853-1, Geneva, Switzerland, 2007.

[72] F. Lacoste, M. Bousquet, L. Castanet, F. Cornet, and J. Lemorton, "Event-based testing analysis of rain attenuation time series synthesizers for the Ka-band satellite propagation channel," in *Proc. CLIMDIFF Conf.*, Sep. 2005.

[73] X. Boulanger, L. Feral, L. Castanet, N. Jeannin, G. Carrie, and F. Lacoste, "A rain attenuation time-series synthesizer based on a dirac and lognormal distribution," *IEEE Trans. Antennas Propag.*, vol. 61, no. 3, pp. 1396–1406, Mar. 2013.

[74] *Specific Attenuation Model for Rain for Use in Prediction Methods*, document ITU-R P.838-3, Geneva, Switzerland, 2005.

[75] *Characteristics of Precipitation for Propagation Modelling*, document ITU-R P.837-7, Geneva, Switzerland, 2007.

[76] *Probability Distributions Relevant to Radiowave Propagation Modelling*, document ITU-R P.1057-6, Geneva, Switzerland, 2019.

[77] J. J. Shynk, *Probability, Random Variables, and Random Processes: Theory and Signal Processing Applications*. Hoboken, NJ, USA: Wiley, 2013.

[78] A. Galántai, "The theory of Newton's method," *J. Comput. Appl. Math.*, vol. 124, nos. 1–2, pp. 25–44, Dec. 2000.

[79] I. S. Gradshteyn and I. M. Ryzhik, *Table of Integrals, Series, and Products*, 6th ed. New York, NY, USA: Academic, 2000.

[80] *The Wolfram Functions Site*. Accessed: Mar. 16, 2022. [Online]. Available: http://functions.wolfram.com/06.27.21.0011.01

ALEXANDROS-APOSTOLOS A. BOULOGE-ORGOS (Senior Member, IEEE) was born in Trikala, Greece, in 1988. He received the Diploma degree in electrical and computer engineering and the Ph.D. degree in wireless communications from the Aristotle University of Thessaloniki (AUTh), in 2012 and 2016, respectively.

In 2017, he joined the Department of Digital Systems, University of Piraeus, where he conducts research in the area of wireless communications. From October 2012 to September 2016, he was a Teaching Assistant with the Department of ECE, AUTh. Since February 2017, he has been serving as an Adjunct Professor with the Department of ECE, University of Western Macedonia; and as an Visiting Lecturer with the Department of Computer Science and Biomedical Informatics and the Department of Computer Science both at the University of Thessaly and with the Department of Computer Science, International Hellenic University, Greece. He has authored and coauthored more than 80 technical articles, which were published in scientific journals and presented at prestigious international conferences. Furthermore, he has submitted two (one national and one European) patents. His current research interests include wireless communications and networks with emphasis in high frequency communications, optical wireless communications, and signal processing and communications for biomedical applications.

Prof. Boulogeorgos has been involved as a member of organizational and technical program committees in several IEEE and non-IEEE conferences and served as a reviewer and a guest editor for various IEEE and non-IEEE journals and conferences. He is a member of the Technical Chamber of Greece. He was awarded the Distinction Scholarship Award from the Research Committee of AUTh, in 2014; and was recognized as an Exemplary Reviewer (top 3% of reviewers) for IEEE COMMUNICATIONS LETTERS, in 2016. He was named as a Top Peer Reviewer (top 1% of reviewers) in cross-field and computer science in the Global Peer Review Awards 2019, which was presented by the Web of Science and Publons. In 2021, he received the Best Oral Presentation Award at the International Conference on Modern Circuits and Systems Technologies (MOCAST) 2021. He is currently an Editor for IEEE COMMUNICATIONS LETTERS and an Associate Editor for the *Frontiers in Communications and Networks* and the *Telecom* (MDPI).

JOSÉ MANUEL RIERA (Senior Member, IEEE) was born in Aviles, Spain, in 1963. He received the M.S. and Ph.D. degrees in telecommunication engineering from the Universidad Politécnica de Madrid (UPM), Spain, in 1987 and 1991, respectively.

Since September 2017, he has been a Professor of radio communications at UPM, where he was previously an Associate Professor, since 1993. He is currently the Leader of the UPM Research Group on Information and Communication Technologies (GTIC), which is integrated in the Information Processing and Telecommunications Center (IPTC). He has been the leader of nearly 50 research projects, funded by private companies, public agencies or national and international research programs, including CE, ESA, and COST. His group contributes regularly to the working parties of ITU-R Study Group 3 (Propagation). He is the author of more than 200 technical papers, more than 130 of them published in international journals, conference proceedings, or as book chapters. His research interests include radiowave propagation and wireless communication systems.

ANGELIKI ALEXIOU (Member, IEEE) received the Diploma degree in electrical and computer engineering from the National Technical University of Athens, in 1994, and the Ph.D. degree in electrical engineering from Imperial College of Science, Technology and Medicine, University of London, in 2000. Since May 2009, she has been a Faculty Member with the Department of Digital Systems, where she conducts research and teaches undergraduate and postgraduate courses in broadband communications and advanced wireless technologies. Prior to this appointment, she was with Bell Laboratories; Wireless Research; and Lucent Technologies (later Alcatel-Lucent, now NOKIA), Swindon, U.K., first as a Member of Technical Staff, from January 1999 to February 2006; and later as the Technical Manager, from March 2006 to April 2009. She is a Professor of broadband communications systems with the Department of Digital Systems, ICT School, University of Piraeus, Greece. Her current research interests include radio interface for 6G systems, MIMO, THz wireless communication technologies, reconfigurable intelligent surfaces, cooperation and coordination for ultra dense wireless networks, "cell-less" architectures, and machine learning for wireless systems. She is a member of the IEEE ComSoc, the IEEE SP Society SAM TC, and the Technical Chamber of Greece; and a Core Member of the IEEE ComSoc SIG on TeraHertz communications and the IEEE SP Society. She was a co-recipient of the Bell Labs President's Gold Award, in 2002, for contributions to Bell Labs Layered Space-Time (BLAST) Project and the Central Bell Labs Teamwork Award, in 2004, for role model teamwork and technical achievements in the IST FITNESS Project. She was the Chair of the Working Group on Radio Communication Technologies and of the Working Group on High Frequencies Radio Technologies of the Wireless World Research Forum. She is the Project Coordinator of the H2020 TERRANOVA Project and the Technical Manager of the H2020 ARIADNE Project.

• • •